https://doi.org/10.5194/egusphere-2026-3458
Preprint. Discussion started: 28 August 2026

Towards robust inversions: Parametric weighting of high-resolution TROPOMI observations for global CH_4 emission estimates with TMVar (TM5-MP/4DVAR)

Santiago Parraguez Cerda[1], Johann Rasmus Nüß[1], Nikos Daskalakis[1], Arjo Segers[2], Oliver Schneising[1], Mihalis Vrekoussis[1,3,4], and Maria Kanakidou[1,5,6]

[1]Institute of Environmental Physics (IUP), University of Bremen, Germany.
[2]Department of Air Quality and Emissions Research, Netherlands Organisation for Applied Scientific Research (TNO), The Netherlands.
[3]Center of Marine Environmental Sciences (MARUM), University of Bremen, Germany.
[4]Climate and Atmosphere Research Center (CARE-C), The Cyprus Institute, Cyprus.
[5]Environmental Chemical Processes Laboratory (ECPL), Department of Chemistry, University of Crete, Greece.
[6]Center for Studies of Air Quality and Climate Change (C-STACC), Foundation for Research and Technology Hellas (FORTH), Greece.

Correspondence: Santiago Parraguez Cerda (sanparra@uni-bremen.de), Nikos Daskalakis (daskalakis@uni-bremen.de), and Maria Kanakidou (mariak@uoc.gr)

Abstract. Satellite observations play a central role in monitoring atmospheric methane (CH_4), a potent greenhouse gas. Recently launched instruments such as TROPOMI provide unprecedented spatial coverage, however, heterogeneous sampling with both dense and sparsely covered regions poses challenges for inverse modeling systems. This uneven sampling can cause very densely observed areas to dominate the inversion and lead to vanishing gradients in sparsely covered regions.

We present a parametric regularization method that computes observation-specific weighting factors based on the spatial and temporal distribution of measurements. Our method modifies the observational covariance matrix through a preprocessing step, homogenizing the effective weight of densely and sparsely sampled regions without introducing additional computational cost during the optimization. Since the parametric weighting is determined prior to the inversion, the approach can be used to calculate weights for multiple-instrument inversions, without further additional parameter tuning. The adaptive regularization is applied to global methane emission inversions for 2019, at $1° \times 1°$ resolution, using the TMVar (TM5-MP/4DVAR v1.2.6 LAMOS) system, assimilating TROPOMI column observations.

Compared to a constant regularization approach, the presented method reduces the relative variation in grid-cell weights by about 20%, by strengthening constraints in high-latitude and oceanic regions. Posterior simulations from inversions that either assimilate satellite data only or also assimilate NOAA surface measurements are evaluated against independent TCCON column observations, showing that the method preserves overall inversion performance while improving the spatial balance of satellite influence. The resulting global methane budget is consistent with recent top-down estimates from the Global Methane Budget.

https://doi.org/10.5194/egusphere-2026-3458
Preprint. Discussion started: 28 August 2026

1 Introduction

Climate change impacts have become increasingly evident in recent decades, largely driven by rising global surface temperatures. This warming is primarily attributed to increasing atmospheric concentrations of greenhouse gases (GHGs) from anthropogenic activities (Eyring et al., 2021). Among them, methane (CH_4) is a major, well-mixed greenhouse gas (WMGHG) with a Global Warming Potential (GWP) of 29.8 (Etminan et al., 2016; Forster et al., 2021) over a 100-year time horizon, making it roughly 30 times more effective than CO_2 at warming the atmosphere over this period.

Since the pre-industrial era, atmospheric CH_4 concentrations have increased by approximately 150% (Kirschke et al., 2013; Saunois et al., 2020), contributing about 0.28 [0.19 – 0.39]°C to global surface warming (Forster et al., 2021). Owing to its atmospheric lifetime of about 9 years (Szopa et al., 2021), reducing CH_4 emissions can produce a rather rapid climate response, which makes methane mitigation an attractive near-term climate strategy.

Methane originates from a combination of natural and anthropogenic sources, including wetlands (29%), agriculture (40%), fossil fuels (20%), and biomass burning (4%) (Saunois et al., 2025). Methane is primarily removed from the atmosphere through oxidation by hydroxyl radicals (OH), which accounts for roughly 90% of its total loss (Kirschke et al., 2013; Saunois et al., 2025). Additional sinks include soil uptake and stratospheric reactions with atomic oxygen ($O(^1D)$) and chlorine radicals (Seinfeld and Pandis, 2016). Despite substantial progress in understanding CH_4 emissions, uncertainties remain in quantifying their regional distribution and temporal variability (Turner et al., 2019). These uncertainties contribute to persistent discrepancies between bottom-up inventories and top-down inversion estimates, although the gap has narrowed in recent years (Saunois et al., 2020, 2025).

Those top-down methods rely on assimilating atmospheric observations into chemical transport models to optimize prior emission estimates. Surface monitoring networks provide highly accurate long-term measurements but are spatially sparse, particularly in the Southern Hemisphere, resulting in strongly uneven data coverage (Dlugokencky et al., 2011; Paton-Walsh et al., 2022). Satellite instruments complement these networks by offering near-global, high-resolution coverage (Jacob et al., 2016, 2022). Earlier missions such as SCIAMACHY and GOSAT established global column monitoring capabilities (Buchwitz et al., 2006; Frankenberg et al., 2006; Kuze et al., 2016), while more recent instruments such as TROPOMI have substantially increased spatial resolution and data density (Veefkind et al., 2012).

The growing volume and heterogeneous distribution of satellite observations pose new challenges for inverse modeling systems. Combining data sources enhances emission constraints by merging the high precision of ground-based measurements with the broad spatial coverage of satellite data (Bergamaschi et al., 2009, 2013; Naus et al., 2022; Krol et al., 2013; Lu et al., 2021). However, in variational inversions, densely sampled regions can dominate the cost function, potentially reducing the influence of sparsely observed areas and ground-based measurements (Kopacz et al., 2010; Hooghiemstra et al., 2012). To mitigate this imbalance, previous studies have applied constant regularization or inflation factors to satellite observations (Hooghiemstra et al., 2012; Krol et al., 2013; Naus et al., 2022; Nechita-Banda et al., 2018; Qu et al., 2021). While effectively reducing overfitting, constant factors do not account for the spatial and temporal clustering of observations and can lead to vanishing gradients in sparsely covered regions. More recent adaptive approaches adjust a single global factor during optimization,

https://doi.org/10.5194/egusphere-2026-3458
Preprint. Discussion started: 28 August 2026

but they still treat all observations within a dataset uniformly and do not explicitly address local sampling density (Nüß et al., 2025). Robustly combining heterogeneous datasets, therefore, requires a regularization strategy that accounts for the spatial and temporal distribution of individual observations without substantially increasing computational cost.

In this study, we introduce a parametric method that computes observation-specific regularization factors from the local density of satellite measurements. Unlike approaches that require selecting a regularization factor or tuning it during the inversion, the proposed method derives the weighting directly from the spatial distribution of the observations in a preprocessing step, thereby removing the need for parameter choices. The weights are calculated prior to the optimization and incorporated into the diagonal of the observational covariance matrix, preserving a fixed covariance structure throughout the inversion. As the weighting relies solely on the observational dataset before assimilation, it is independent of the inversion algorithm and does not depend on the model configuration. This approach homogenizes the effective influence of densely and sparsely sampled regions while remaining computationally efficient. Furthermore, it facilitates the integration of multiple observational datasets within the same inversion framework, either by calculating factors per dataset or by combining them to account for all data simultaneously. We apply the method to global CH_4 emission inversions for 2019 at $1^\circ \times 1^\circ$ resolution using the TM5-MP/4DVAR system and TROPOMI column observations. Through a series of experiments comparing constant and adaptive regularization approaches, and by combining satellite observations with NOAA surface measurements, we assess the impact of the proposed scheme on emission estimates and evaluate the results against independent TCCON column observations.

2 Methodology

2.1 Transport model description

Global CH_4 concentrations are simulated using the Eulerian chemical transport model TM5-MP (Krol et al., 2005; Williams et al., 2017). The model is configured at a horizontal resolution of $1^\circ \times 1^\circ$ with 34 hybrid sigma–pressure vertical levels extending from the surface to 0.01 hPa.

Atmospheric transport is driven by meteorological fields from the ERA5 reanalysis produced by the European Centre for Medium-Range Weather Forecasts (ECMWF; Hersbach et al., 2020). ERA5 provides 3-hourly meteorological data (hourly at the surface) at a native horizontal resolution of approximately 31 km with 137 vertical levels extending from the surface to 1 Pa. For use in TM5-MP, these fields are horizontally averaged to the model grid, vertically reduced to 34 layers, and temporally interpolated to the internal model timestep.

Methane chemical loss is represented using a simplified oxidation scheme that accounts for main atmospheric sinks, namely OH radicals, $Cl^\cdot$ and $O(^1D)$. The chemical destruction of CH_4 by OH radicals in the troposphere is simulated using monthly averaged OH fields that combine the ECMWF Copernicus Atmosphere Monitoring Service (CAMS) global reanalysis (EAC4; Inness et al. (2019)) with dedicated IFS/CB05/BASCOE simulations (Huijnen et al., 2016). A factor of 1.1 scales tropospheric OH concentrations to ensure consistency with methyl chloroform (MCF) simulations, following Naus et al. (2021) and the configuration used in CAMS CH_4 inversions (Segers et al., 2025). In the stratosphere, monthly climatological fields of OH, $O(^1D)$, and $Cl^\cdot$ from the same IFS/CB05/BASCOE simulations are applied, consistent with the CAMS setup (Segers et al.,

https://doi.org/10.5194/egusphere-2026-3458
Preprint. Discussion started: 28 August 2026

2025). All reaction rates are calculated using monthly mean temperature fields, consistent with the temporal resolution of the prescribed oxidant concentrations (OH, $O(^1D)$, and $Cl^{\cdot}$). These oxidant fields remain fixed throughout all inversions and are not included in the optimized state vector.

2.2 4DVar assimilation method

The four-dimensional variational (4DVar) data assimilation technique (Talagrand and Courtier, 1987) is widely used for inverse modeling of atmospheric trace gases (Eskes et al., 1999; Hooghiemstra et al., 2011; Bergamaschi et al., 2013; Nüß et al., 2025). This method seeks to iteratively determine an optimal state vector $\mathbf{x}$ that reproduces a set of atmospheric observations $\mathbf{y}$ within a specified time window, while remaining consistent with prior information. In this study, the state vector $\mathbf{x}$ consists of multiplicative scaling factors applied to prior surface CH_4 emissions, optimized independently for each emission category. The state vector is related to the modeled observations by simulating $\mathbf{y}$ through a nonlinear forward operator $\mathbf{H}$, represented as

$$\mathbf{y} = \mathbf{H}(\mathbf{x},\mathbf{p}) + \varepsilon_O \quad , \tag{1}$$

where $\mathbf{p}$ denotes model parameters that are not subject to correction and ε_O represents the observational error. This error term includes instrument, representativeness, and model representation errors, which are assumed to be uncorrelated.

From a Bayesian perspective, the inverse problem consists of estimating the posterior probability density $P(\mathbf{x}|\mathbf{y})$ given prior information $\mathbf{x}_a$. We assume that (i) the prior errors $(\mathbf{x}-\mathbf{x}_a)$ and the observational errors ε_O are unbiased and Gaussian distributed with covariance matrices $\mathbf{B}$ and $\mathbf{R}$, respectively, and (ii) prior and observational errors are statistically independent. Under these assumptions, maximizing the posterior probability is equivalent to minimizing the cost function J defined as

$$\begin{aligned} J(\mathbf{x}) = &(\mathbf{x}-\mathbf{x}_a)^T\mathbf{B}^{-1}(\mathbf{x}-\mathbf{x}_a) + \\ &(\mathbf{H}(\mathbf{x})-\mathbf{y})^T\mathbf{R}^{-1}(\mathbf{H}(\mathbf{x})-\mathbf{y}) \quad , \end{aligned} \tag{2}$$

where the first term represents the deviation from the prior (background term), and the second term the mismatch between modeled and observed concentrations (see also Chapter 11 of Brasseur and Jacob (2017)). The background error $\mathbf{B}$ is constructed using the uncertainty of the parameters in the state vector, and their correlation in space and time.

In this work, the observational covariance matrix $\mathbf{R}$ is modified through an observation-specific weighting matrix $\mathbf{\Gamma}$ (Section 2.3).

The optimality condition is obtained by setting the gradient of J to zero:

$$\nabla J(\mathbf{x}) = 2\mathbf{B}^{-1}(\mathbf{x}-\mathbf{x}_a) + 2\mathbf{K}^T\mathbf{R}^{-1}(\mathbf{H}(\mathbf{x})-\mathbf{y}) = 0 \quad , \tag{3}$$

where $\mathbf{K} = \nabla_{\mathbf{x}}\mathbf{H}$ denotes the Jacobian matrix of the forward model. Due to the nonlinearity of $\mathbf{H}$ and the large dimension of $\mathbf{x}$, an analytical solution is computationally unfeasible. The cost function J is therefore minimized iteratively using a gradient-based optimization algorithm. The adjoint model, represented by $\mathbf{K}^T$, is computed implicitly through backward time integration of the adjoint operator $(\partial\mathbf{y}_p/\partial\mathbf{y}_{p-1})^T$. At each iteration, the adjoint propagates the adjoint forcing $\mathbf{R}^{-1}(\mathbf{H}(\mathbf{x})-\mathbf{y})$

https://doi.org/10.5194/egusphere-2026-3458
Preprint. Discussion started: 28 August 2026

backward in time, obtaining the gradient of J with respect to emissions at earlier time steps. The resulting gradient vector is then passed to the optimizer to update $\mathbf{x}$.

The Hessian of the cost function is given by

$$\nabla^2 J(\mathbf{x}) = 2\mathbf{B}^{-1} + 2\mathbf{K}^T\mathbf{R}^{-1}\mathbf{K} \quad . \tag{4}$$

Explicit computation or inversion of the Hessian is computationally prohibitive for the high-dimensional state vector considered here, particularly since $\mathbf{K}$ and $\mathbf{K}^T$ are not formed explicitly. Consequently, posterior error covariance estimates are not provided, which limits the quantitative assessment of the uncertainty in the optimized emissions and of the spatial and temporal distribution of the posterior constraints. This limitation concerns the uncertainty associated with the absolute emission estimates and with differences between individual optimized solutions. It does not, however, preclude the comparative analysis performed here, which focuses on the response of the inversion to a different observational weighting configuration. In particular, the weighting schemes produce systematic spatially and seasonally structured changes in the effective observational weights (Section 3.2), allowing their impact on the optimized emission estimates to be examined directly. The results should therefore be interpreted based on the relative effect of the weighting rather than as a quantitative assessment of posterior emissions.

The adjoint implementation of TM5-MP used in this study follows the framework described by Meirink et al. (2008). Minimization of Eq. 2 is carried out using the M1QN3 quasi-Newtonian optimization algorithm (Gilbert and Lemaréchal, 1989), a limited-memory method well suited for large, under-constrained problems without requiring explicit construction of the full Hessian matrix.

2.3 Regularization factor

Recent satellite instruments provide global coverage with increasingly high spatial resolution and sampling frequency. While this improves observational constraints, it also introduces large disparities in the number and spatial distribution of observations among datasets. As shown by Kopacz et al. (2010), when products from multiple satellites (MOPITT, AIRS, and SCIAMACHY) are assimilated simultaneously, inversion results can become strongly biased toward the instrument with the highest observation density. In practice, the overwhelming number of soundings from a single product may dominate the cost function and reduce the relative influence of other information sources, i.e., other datasets or the prior.

A common strategy to mitigate this imbalance is to apply covariance regularization (or inflation), which increases the observational error covariance matrix $\mathbf{R}$ for the denser datasets. When dense observations are not fully independent, reducing their effective weight in the cost function can limit overfitting by correcting for underestimated uncertainties or neglected error correlations. More fundamentally, covariance inflation accounts for the mismatch between the (relatively) coarse spatial resolution of the model, and the much finer sampling of satellite observations. When multiple observations fall within a region not resolved by the model grid, unresolved sub-grid variability can induce correlated representativeness errors, so these observations may provide less independent information than assumed if their errors are treated as uncorrelated. In such cases, treating these observations as independent leads to an overestimation of the effective information content, resulting in an excessive

https://doi.org/10.5194/egusphere-2026-3458
Preprint. Discussion started: 28 August 2026

contribution to the cost function. Inflating $\mathbf{R}$, therefore, acts as a practical approximation when these error correlations are not represented explicitly in the observation error covariance matrix, helping to prevent densely sampled observations from dominating the inversion beyond what is justified by their effective information content.

Previous studies have typically implemented constant inflation factors selected heuristically. These scalar factors I are applied directly to inflate the matrix $\mathbf{R}$. For example, Chevallier (2007) applied an inflation factor of 2 to OCO CO_2 retrieval errors, while Hooghiemstra et al. (2012) used a larger value ($I = \sqrt{50}$) for MOPITT observations following sensitivity analyses. Similar values were adopted in subsequent CO inversion studies (Nechita-Banda et al., 2018; Naus et al., 2022). Alternative formulations introduce a regularization factor γ directly in the observational term of the cost function (Brasseur and Jacob, 2017), which is mathematically equivalent to inflating $\mathbf{R}$ when $\gamma = I^{-1}$.

For methane inversions, the choice of γ has often relied on L-curve analyses (Hansen, 2000). Reported values vary substantially depending on model resolution and dataset characteristics (Zhang et al., 2018; Lu et al., 2021; Qu et al., 2021), showing the absence of a universally optimal constant factor. Some of these values have subsequently been adopted in similar inversion configurations (Maasakkers et al., 2019; Zhang et al., 2021).

Several approaches have been proposed to address this limitation. For instance, Liu and Rabier (2003) suggested weighting the cost function by the number of observations to account for spatially correlated errors. More recently, Simonin et al. (2019) introduced a statistical method that accounts for spatial error correlations based on distances between clusters of observations. However, this approach becomes computationally prohibitive for the large covariance matrices involved in variational inversions of satellite datasets, as the matrices must be recomputed at every iteration. Another strategy was proposed by Nüß et al. (2025), who adaptively adjusted a single global inflation factor so that the satellite contribution to the cost function roughly matches that of in-situ observations. Although this improves robustness at the cost function level, it still applies the same weight to all observations and does not account for local spatial or temporal clustering.

Here, we introduce an observation-specific regularization approach in which each satellite observation receives an individual weight based on the local sampling density. The regularization factors are computed once during a preprocessing step and remain fixed throughout the inversion, preserving a consistent covariance structure while avoiding additional computational cost during the minimization. Specifically, weighting each observation allows for a heterogeneous treatment of satellite data. This parametric formulation makes the approach straightforward to use when combining multiple observational datasets, since the weights depend only on the sampling characteristics of the observations themselves.

This framework can also be applied to super-observations. Since the method fundamentally relies on the spatial distribution and local density of nearby observations, it can extend to aggregated observations constructed from multiple soundings or retrievals. In this case, the weighting is applied to either the super-observations themselves or to the individual pixels to be aggregated, while still reflecting the underlying sampling geometry and spatial representativeness of the original observations. This aligns with recent work emphasizing the importance of accounting for spatial correlations and representation errors in super-observation-based applications (e.g. Nüß et al., 2025; Rijsdijk et al., 2025).

The method relies on an unnormalized kernel density estimator for each observation using a Gaussian kernel applied to pairwise Haversine distances d_{ij} [rad] among observations within a temporally constrained neighborhood. For each observation

https://doi.org/10.5194/egusphere-2026-3458
Preprint. Discussion started: 28 August 2026

i, the inverse regularization factor is defined as

$$\gamma_i^{-1} = \sum_{j=1}^{N} \exp\left(-\frac{d_{ij}^2}{2h^2}\right) \quad , \tag{5}$$

where h [-] denotes the bandwidth parameter, and N the number of observations considered within the local neighborhood. In matrix form this becomes

$$\boldsymbol{\gamma}^{-1} = \exp\left(-\frac{\mathbf{D}^2}{2h^2}\right)\mathbf{1}_N \quad ,$$

with $\mathbf{D} = [d_{ij}]$ and $\mathbf{1}_N$ an all-ones vector.

By construction, isolated observations yield $\gamma_i = 1$, resulting in no inflation, whereas densely clustered observations receive stronger inflation (i.e., larger values of γ_i^{-1}). This formulation approximates the influence of unresolved spatial correlations arising from the mismatch between observation density and model resolution, while maintaining a diagonal observational covariance matrix and thereby avoiding the computational burden associated with explicitly constructing correlated errors. The underlying assumption is that densely sampled regions contain more observations that are not independent at the model spatial scale; increasing their observational uncertainty therefore reduces their aggregate influence without explicitly specifying a spatial correlation structure.

The bandwidth h controls the spatial smoothing of the density estimate. Instead of prescribing a spatial length for smoothing, we use Silverman's (1986) rule to estimate a bandwidth, which accounts for the number of observations and the spread of the data, yielding $h = 0.2$ [rad], which translates roughly to $11.5°$. The magnitude of the used h represents the reach of the effect of an observation for the density estimation. This choice provides sufficiently smooth density estimates while avoiding excessively localized variations in the resulting weights. Although Silverman's rule can oversmooth the resulting estimates, sensitivity tests (see Figures S3 and S4) indicate that this relatively large bandwidth provides a useful conservative starting point for the inversion. Nevertheless, more tailored bandwidth selection methods, such as the approach of Sheather and Jones (1991), could be considered in future work when aiming for a better representation of the empirical density distribution of observations. The use of more localized density estimates would require a more careful assessment of their impact on the inversion.

To reduce computational cost, each satellite orbit is divided into 15-minute scanning bands. Density estimates for each pixel are computed using observations within the same band and the two adjacent bands. Sensitivity tests showed negligible differences when extending the temporal window (see Figure S3), while substantially increasing computational expense.

Although not explicitly optimized for the cost function minimization, the bandwidth is deterministically calculated from the observation set, avoiding the need for any manual parameter tuning for the density estimation. Once computed, the regularization vector $\boldsymbol{\gamma}$ is used to modify the covariance matrix,

$$\mathbf{R}^* = \mathrm{diag}(\boldsymbol{\gamma}^{-1})\,\mathbf{R} \quad . \tag{6}$$

https://doi.org/10.5194/egusphere-2026-3458
Preprint. Discussion started: 28 August 2026

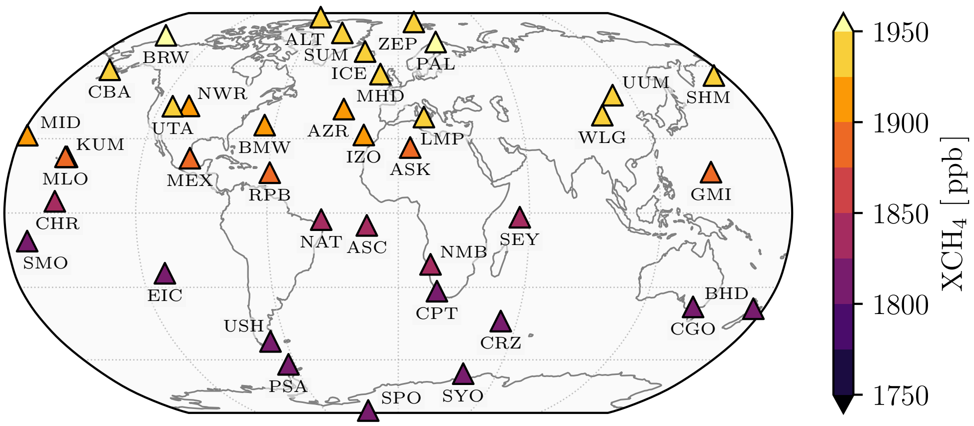

Figure 1. Map of NOAA stations used in this study and CH_4 average mixing ratios measured during 2019.

A limitation of the approach is that representativeness effects are accounted for only indirectly through density-based inflation rather than explicit covariance modeling. Nevertheless, this simplification allows the method to scale efficiently to the large observational datasets typically used in 4DVar inversions.

2.4 Atmospheric observations

2.4.1 Surface measurements

Surface measurements of CH_4 mixing ratios were obtained from the global NOAA station network (Dlugokencky et al., 1994, 2009). Flask samples are collected approximately weekly, reporting the dry mole fraction of CH_4 together with the corresponding measurement uncertainty. Among the available stations, only background sites are used for this study. The horizontal resolution of the model ($1^\circ \times 1^\circ$) does not allow a full capture of the heterogeneous distribution and strong gradients near large methane sources, which can lead to significant representativeness errors. Consequently, stations influenced by localized or short-term emission events are excluded, and only background stations affected by diffuse, persistent, or seasonal emissions are retained. For this study, a subset of 39 stations was selected from the 53 sites providing data during the simulation period (see Figure 1 and Table S1). This selection follows an approach similar to Hooghiemstra et al. (2012), excluding stations with high variability.

Station selection is performed using a Seasonal-Trend decomposition with LOESS (STL; Cleveland et al., 1990), which separates each time series into a trend, seasonal cycle, and residual component. For each station, the trend is estimated using a 10-year smoother and the seasonal component using a 1-year smoother. The residual is then calculated as the difference between the original series and the sum of the trend and seasonal components. We quantify the variability by computing the standard deviation of the residuals normalized by the observed values. Stations with an average relative deviation larger than 1% are excluded. As an additional diagnostic, the autocorrelation of each time series is evaluated. Higher autocorrelation typically

https://doi.org/10.5194/egusphere-2026-3458
Preprint. Discussion started: 28 August 2026

indicates well-mixed background conditions or influence from a stationary source, since only small weekly variations in mixing ratios are expected. Stations retained in the final dataset exhibit strong temporal persistence, whereas excluded stations show a rapid decline in autocorrelation between consecutive observations.

When multiple samples are collected simultaneously at the same site, a weighted mean mixing ratio and uncertainty are calculated using the reported measurement errors. A minimum measurement error of 3.0 ppb is imposed to account for the limitation of numerical models to fully represent subgrid variability and point measurements (Bergamaschi et al., 2005; Meirink et al., 2008). These values are then used directly in the calculation of the cost function during the inversions and for comparisons with model results. The standard deviation of simultaneous measurements is also computed and later used to estimate representativeness errors.

The error-weighted mean and variance for multiple measurements (i.e., sharing the same timestamps) are calculated assuming a conservative correlation between measurement errors $\rho = 0.15$, preventing a significant underestimation of the resulting variance. Using the reported uncertainties, this assumption allows reconstruction of the correlation matrix Σ for a set of measurements $\mathbf{x}_*$ and the calculation of unbiased estimators for the weighted mean mixing ratio $\bar{x}_*$ and its variance $\bar{\sigma}_*^2$.

$$\bar{x}_* = \frac{\mathbf{1}^T \Sigma^{-1} \mathbf{x}_*}{\mathbf{1}^T \Sigma^{-1} \mathbf{1}}\,, \qquad \bar{\sigma}_*^2 = \frac{1}{\mathbf{1}^T \Sigma^{-1} \mathbf{1}} \tag{7}$$

2.4.2 Satellite column observations

To test the parametric regularization factor, CH_4 column observations retrieved by the TROPOspheric Monitoring Instrument (TROPOMI; Veefkind et al. (2012)) are used. Launched in 2017 onboard the Sentinel-5 Precursor satellite, TROPOMI measures CH_4 in the short-wave infrared (SWIR) band. The spatial resolution at nadir improved from 7×7 km^2 to 5.5×7 km^2 following an update to the operational settings of the instrument in August 2019. Therefore, the analysis period includes both configurations, although the majority of observations correspond to the earlier resolution. The instrument provides daily global coverage, representing a significant improvement over earlier satellite missions (Lorente et al., 2021). The satellite follows a sun-synchronous orbit with a nominal daytime equatorial crossing time of approximately 13:30 local solar time. As a result, most observations correspond to early afternoon conditions, although additional overpasses occur at high latitudes and during nighttime. These observations capture large-scale seasonal and long-range transport patterns as well as localized emission events. They, therefore, provide valuable information to complement the spatially sparse in-situ measurements used in inversion systems.

In this work, the Weighting Function Modified DOAS (WFMD) retrieval product (Schneising et al., 2019) is used (see Figure 2). This product offers improved spatial coverage, particularly at high latitudes, and provides more realistic uncertainty estimates compared to the operational product (Schneising et al., 2023; Lindqvist et al., 2024). The WFMD v2.0 dataset used here also includes enhanced quality filtering and improved accuracy relative to earlier versions (Schneising et al. (2026)).

To assimilate these satellite observations within our 4DVAR framework, a simulated retrieval is calculated for each sounding. The modeled atmospheric profile is first interpolated to the pixel location and mapped onto the a priori layers of the satellite retrieval. Then, the concentrations at each layer are combined with the provided averaging kernels to compute a modeled total

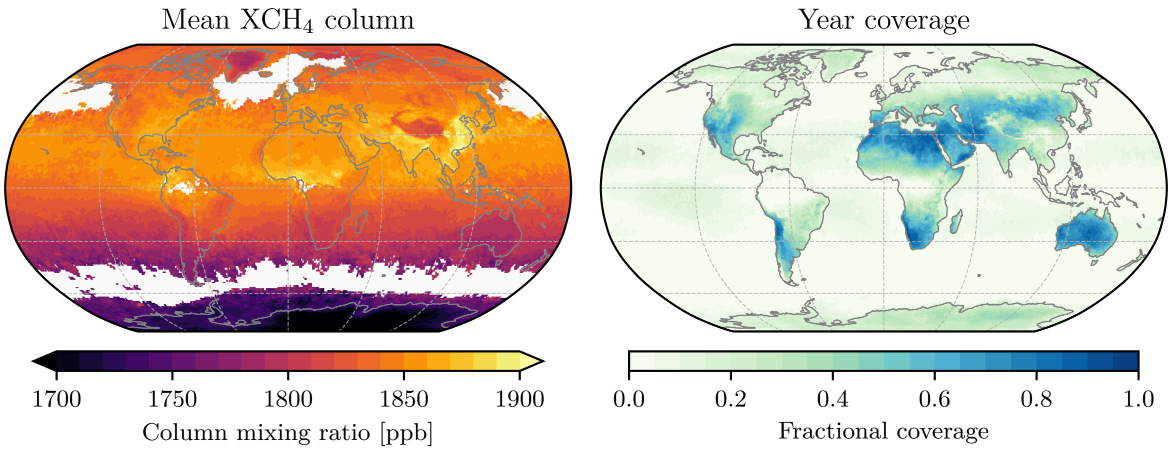

Figure 2. Observations retrieved by the WFMD v2.0 product of TROPOMI for 2019. On the left (a) the annual mean total column mixing ratio of CH_4, and on the right (b) the fraction of days of the year with at least a single valid observation in the grid. Both binned to a $1° \times 1°$ grid.

column. This simulated retrieval is subsequently compared with the observed column value, providing the cost contribution and adjoint forcing used during the inversion.

2.4.3 Ground-based column observations

In addition to comparisons with NOAA surface measurements and TROPOMI observations, the simulated mixing ratios obtained from the optimized emissions are evaluated using independent ground-based observations from the Total Carbon Column Observing Network (TCCON; Wunch et al. (2011)). TCCON consists of a global network of Fourier Transform Spectrometers measuring direct solar spectra in the near-infrared region, providing highly accurate observations of total column mixing ratios for several trace gases, including CH_4. These observations are not assimilated in any experiment and are used exclusively for independent evaluation.

During the simulation period, 25 TCCON sites were operational, providing CH_4 density columns (see Table S2). Figure 3 shows the TCCON sites used in this study together with the mean total column mixing ratio of CH_4 observed during 2019. Some sites are located near emission regions and, therefore, cannot be considered pure background locations. Consequently, the model may have greater difficulty reproducing the variability observed at some of these sites.

To compare modeled concentrations with TCCON observations, a simulated total column must be calculated by sampling the model output and accounting for the vertical sensitivity of the instrument. Following the recommendations in the TCCON documentation, averaging kernels are applied together with a pressure weighting function to compute a modeled total column mixing ratio (Wunch et al., 2010).

$$\hat{X} = \frac{\sum_j \left(a_k\left(\hat{x} - x_p\right) + x_p\right)_j \cdot \tau_j}{\sum_j \tau_j} \quad . \tag{8}$$

https://doi.org/10.5194/egusphere-2026-3458
Preprint. Discussion started: 28 August 2026

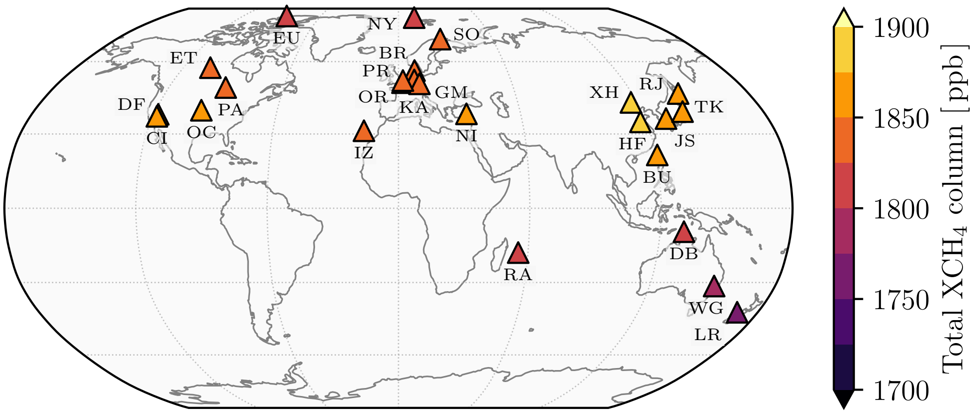

Figure 3. Map of TCCON sites used in this study after filtering with the mean total column mixing ratio of CH_4 observed during 2019.

Here, $\hat{X}$ denotes the simulated total column mixing ratio, a_k the averaging kernel, $\hat{x}$ the simulated mixing ratio for layer j, x_p the corresponding a priori value, and τ_j the pressure weighting factor.

Since the provided observation a priori mixing ratios are expressed relative to wet air, the dry-air mixing ratio must first be calculated by removing the contribution of water vapor:

$$X_{\text{gas}}^{\text{dry}} = X_{\text{gas}}^{\text{wet}} \,/\, \left(1 - X_{H_2O}^{\text{wet}}\right) \quad . \tag{9}$$

Additionally, the pressure weighting factor τ_j is calculated following the formulation of Connor et al. (2008), which allows determination of the weighting factors even when level boundaries are not explicitly provided.

$$\begin{aligned} \tau_j = & \left| \left(-p_j + \frac{p_{j+1} - p_j}{\ln\left(p_{j+1}/p_j\right)}\right) \right. \\ & \left. + \left(p_j - \frac{p_j - p_{j-1}}{\ln\left(p_j/p_{j-1}\right)}\right) \right| \cdot \frac{1}{p_{\text{surf}}} \quad . \end{aligned} \tag{10}$$

TCCON measurements are typically collected in short bursts (as short as every 5 seconds), separated by gaps of several days. Because the model output has a temporal resolution of 15 minutes, this sampling pattern can lead to an over-representation of certain time periods in the comparison. To mitigate this effect, observations occurring within a 15-minute window are averaged using Eq. 7. This temporal aggregation better matches the model resolution and reduces representativeness biases associated with temporal interpolation.

2.5 Experiments performed

We designed a set of experiments to evaluate the impact of the parametric regularization factor and to compare it with the constant values commonly used in previous studies. All experiments consist of two-year inversions performed with the TM5-MP/4DVAR system, including six-month spin-up and spin-down periods. The spin-up period is required to avoid large emission

https://doi.org/10.5194/egusphere-2026-3458
Preprint. Discussion started: 28 August 2026

Table 1. Summary of performed inversions.

Code	Assimilated data	Regularization
S0	none (a priori)	-
S1	stations	-
S2	satellite	constant
S3	satellite	adaptive
S4	stations and satellite (combined)	constant
S5	stations and satellite (combined)	adaptive

adjustments caused by potential biases in the initial emissions and atmospheric concentrations provided to the model. The spin-down period allows the final months of the simulation to remain constrained by subsequent atmospheric observations. The simulations cover the period from July 2018 to June 2020, while the analysis focuses on the 2019 calendar year. This period was selected because the TROPOMI WFMD product has been consistently available since mid-2018.

The experiments differ in the combination of assimilated observations and, when satellite data are used, in the choice of regularization. The baseline inversion (S1) assimilates only surface measurements from the selected NOAA background sites. Satellite-only inversions (S2, S3) are performed using either a constant regularization factor ($\gamma = 0.01$) or the parametric regularization method proposed in this study. Combined inversions (S4, S5), which assimilate both satellite and station data, are carried out using the same two regularization approaches. In addition, the a priori simulation without any data assimilation (S0) is included as a reference.

Altogether, this setup results in six simulations (Table 1), all following the configuration described in Section 2.5.1. The constant value $\gamma = 0.01$ is selected within the range reported by Zhang et al. (2018), who found values between 0.01 and 0.1 to be optimal for their methane inversion setup. Specifically, the lower bound is chosen to better match the mean value of the density-based regularization factors (≈ 0.008), allowing a more direct comparison between the two approaches.

2.5.1 Simulation setup

We separate emissions by source in wetlands, rice, biomass burning, and other sources, since they have distinct spatial patterns and seasonal cycles (Bergamaschi et al., 2010, 2013). This approach isolates emissions with unique temporal behaviors, such as rice (highly seasonal) versus industrial sources (relatively stable). We follow the approach of Bergamaschi et al. (2013) to compile emission inventories, with major updates on anthropogenic, biomass burning, and wetland sources. A summary of the inventories used is presented in Table 2 listing all emission sources and their data resolution.

Anthropogenic emissions come from the Emission Database for Global Atmospheric Research (EDGAR v7.0; Crippa et al. (2021)), which provides monthly estimates by sectors from 1971 to 2021. Rice emissions are separated from other anthropogenic sources due to their significant seasonal cycle, unlike other anthropogenic sources that remain relatively constant throughout the year. Biomass-burning emissions are obtained from the Global Fire Assimilation System (GFAS; Di Giuseppe

https://doi.org/10.5194/egusphere-2026-3458
Preprint. Discussion started: 28 August 2026

Table 2. Methane sources and sinks included in prior emissions, with their original spatial and temporal resolution.

Type	Source	Dataset	Temp. res.	Spat. res.
Anthropogenic	all sources	EDGAR v7.0	monthly	$0.1^{\circ} \times 0.1^{\circ}$
Biomass burning	wildfires	GFAS v1.2	daily	$0.1^{\circ} \times 0.1^{\circ}$
Natural	wetlands	LPJ-WSL	monthly	$0.5^{\circ} \times 0.5^{\circ}$
	oceans	climatological	-	$1.0^{\circ} \times 1.0^{\circ}$
	wild animals	climatological	-	$1.0^{\circ} \times 1.0^{\circ}$
	termites	climatological	-	$1.0^{\circ} \times 1.0^{\circ}$
	geological	not included		
	soil uptake	climatological	-	$1.0^{\circ} \times 1.0^{\circ}$

et al. (2018)), which estimates daily emissions from satellite-derived fire radiative power (FRP). These estimates are then aggregated into monthly emissions for the inversion. For wetland emissions, we use updated simulations from LPJ-WSL runs (Zhang et al., 2016, 2023), a process-based dynamic global vegetation model developed for carbon cycle applications. This dataset provided monthly emissions data from 2000 to 2021. Emissions from oceans (Lambert and Schmidt, 1993) and wild animals have been compiled by Houweling et al. (1999) through extrapolations of measurements and are treated as climatological sources. Termite emissions come from the CAMS global emissions dataset (Doubalova and Sindelarova, 2018), which revises earlier estimates by Sanderson (1996) for 2000. This monthly estimation is also treated as climatological. We excluded geological sources due to high uncertainty in their spatial distribution and magnitude, making it challenging to assess their regional impact. However, we acknowledge the efforts made by Etiope et al. (2019) in creating an emission inventory that may be considered in future studies. A process-based model for estimating soil CH_4 consumption was developed by Ridgwell et al. (1999). In this study, the values from that model are used as climatological, based on the assumption that soil uptake fluxes are influenced more by changes in agricultural practices than by global warming. All emissions are aggregated to the model $1^{\circ} \times 1^{\circ}$ grid, and monthly averages are computed for use in the simulations.

In our simulations, the state vector comprises individual scaling factors for the prior emissions. A single scaling factor is independently assigned to each grid cell at the model's spatial resolution, source category, and month, resulting in 6,220,800 parameters to be optimized in $\mathbf{x}$. The adjoint emission factors are applied using a semi-exponential description for the probability distribution of prior emissions, which ensures that the scaling factors remain positive (Bergamaschi et al., 2009). The optimization is terminated when the gradient of the cost function falls below 10^{-10}, with a maximum of 50 iterations.

To construct the matrix $\mathbf{B}$, spatial correlations are represented by an isotropic Gaussian function for all source categories. Temporal correlations are represented by exponential decay for anthropogenic and natural sources, while rice, biomass burning, and wetlands are assumed to be temporally uncorrelated, following the setup used in CAMS CH_4 inversions (Segers et al., 2025). For the matrix $\mathbf{R}$, the provided uncertainty for each observation is used, and the observation errors are assumed to be

https://doi.org/10.5194/egusphere-2026-3458
Preprint. Discussion started: 28 August 2026

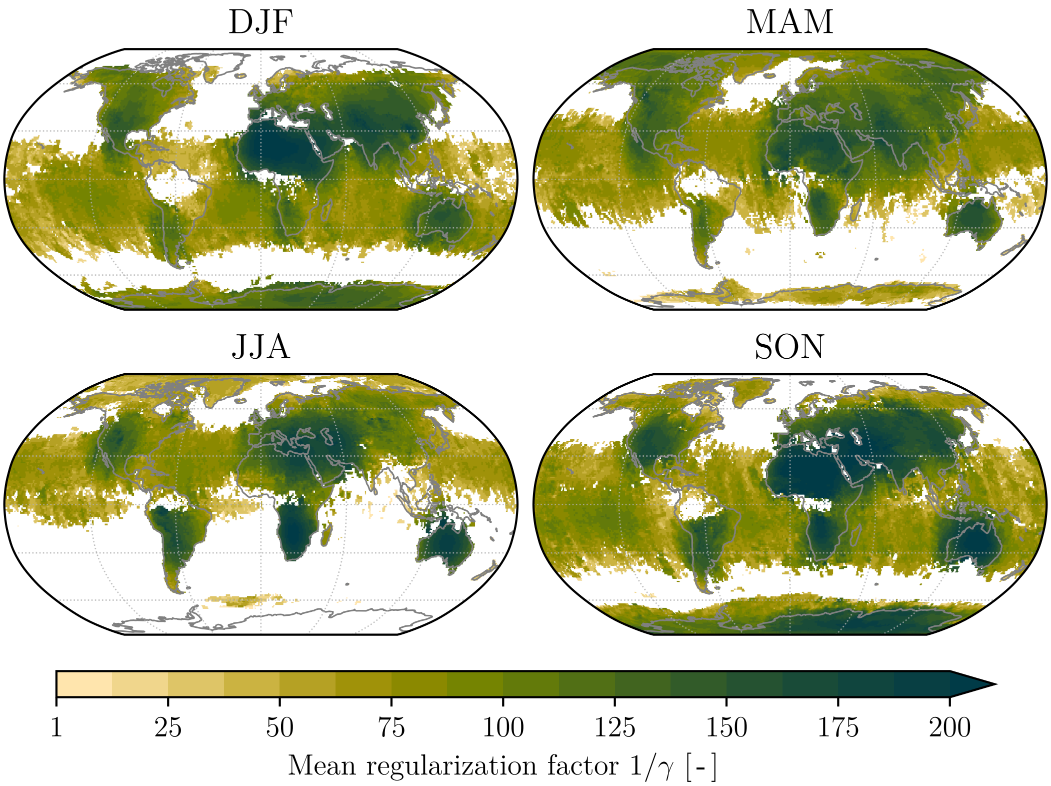

Figure 4. Regularization factor γ for TROPOMI WFMD v2.0 (2019). Individual observation factors are binned into the $1^\circ \times 1^\circ$ grid and averaged seasonally. A value of $\gamma^{-1} = 1$ means no weight reduction. The reciprocal form (γ^{-1}) is shown, such that larger values represent stronger variance inflation.

uncorrelated. A minimum observation error of 3 ppb is imposed to avoid overfitting and to account for the representativeness error of the model. Thus, $\mathbf{R}$ is constructed as a diagonal matrix and subsequently inflated using the weighting matrix Γ. Finally, an estimate of the spatial and temporal transport errors from the a priori runs is added to the matrix.

3 Results and Discussion

3.1 Regularization factor

We compute the parametric regularization factor for each TROPOMI observation before performing the inversions. To evaluate how it varies spatially and seasonally, we aggregate the per-observation factors to the $1^\circ \times 1^\circ$ model grid and average them per season. Figure 4 shows the reciprocal form (γ^{-1}), such that larger values correspond to stronger variance inflation and thus less weight for individual observations.

https://doi.org/10.5194/egusphere-2026-3458
Preprint. Discussion started: 28 August 2026

The spatial distribution of γ^{-1} matches the coverage characteristics of TROPOMI . Areas with persistent and dense coverage throughout the year tend to have larger values, indicating a down-weighting of clustered observations. On the other hand, regions with frequent cloud cover, oceanic areas, and high latitudes during their respective winter seasons, have lower coverage, resulting in values close to 1. This behavior indicates that sparsely covered regions suffer little to no inflation.

A clear seasonal cycle in γ is driven by changes in observational availability between summer and winter periods. Reduced solar illumination and increased cloud cover during winter months decrease the number of successful retrievals, thereby lowering the inflation factors. Conversely, more favorable retrieval conditions during summer months increase local sampling density, resulting in stronger variance inflation and a reduced individual weight of each observation, as contrast to the aforementioned winter months.

Overall, the resulting patterns are consistent with the expected behavior from the kernel density estimation method, in which high-density clusters produce larger estimated densities and therefore stronger regularization, while isolated observations retain most of their weight. No artificial features or discontinuities are introduced, indicating that the selected bandwidth provides a smooth regularization without fully homogenizing the field.

3.2 Weight contribution

Before analyzing the impact of the proposed adaptive regularization on inferred methane emissions, we examine how it redistributes the relative influence of satellite observations compared with a constant regularization approach. To quantify the effect of parametric regularization on the relative weight of each grid cell, we compute the regularization-weighted number of pixels per grid cell and normalize it by the global total. This normalization allows a direct comparison between configurations with different regularization magnitudes.

Figure 5 shows the seasonally averaged distributions. Adaptive regularization produces a clear redistribution of weights, with a general decrease over land, and an increase over the oceans. This behavior reflects the higher observational density over land surfaces, and the limited availability of valid retrievals over oceans, primarily due to low-surface albedo. High-latitude regions in the Northern Hemisphere (NH) receive increased relative cell weight, consistent with the reduced number of observations caused by seasonal darkness.

The primary objective of introducing the adaptive regularization is to achieve a more homogeneous spatial distribution of observational weights across the model grid. To quantify this effect, we compute the coefficient of variation (CV), defined as the ratio of the standard deviation to the mean weight across all grid cells. For 2019, the CV decreases from 1.62 in the constant regularization configuration (independent of the absolute value of γ) to 1.30 when using the adaptive approach (Table 3). This corresponds to an approximately 20 % reduction in relative variation, indicating a substantially less dispersed weight distribution.

Despite the overall reduction, overland regions continue to receive the highest relative weight, as the adaptive parametrization compresses the range of weights without altering the underlying spatial pattern. An increase in cell weight effectively raises the adjoint forcing in those grid cells, thereby mitigating vanishing gradient effects in sparsely covered regions. These changes

https://doi.org/10.5194/egusphere-2026-3458
Preprint. Discussion started: 28 August 2026

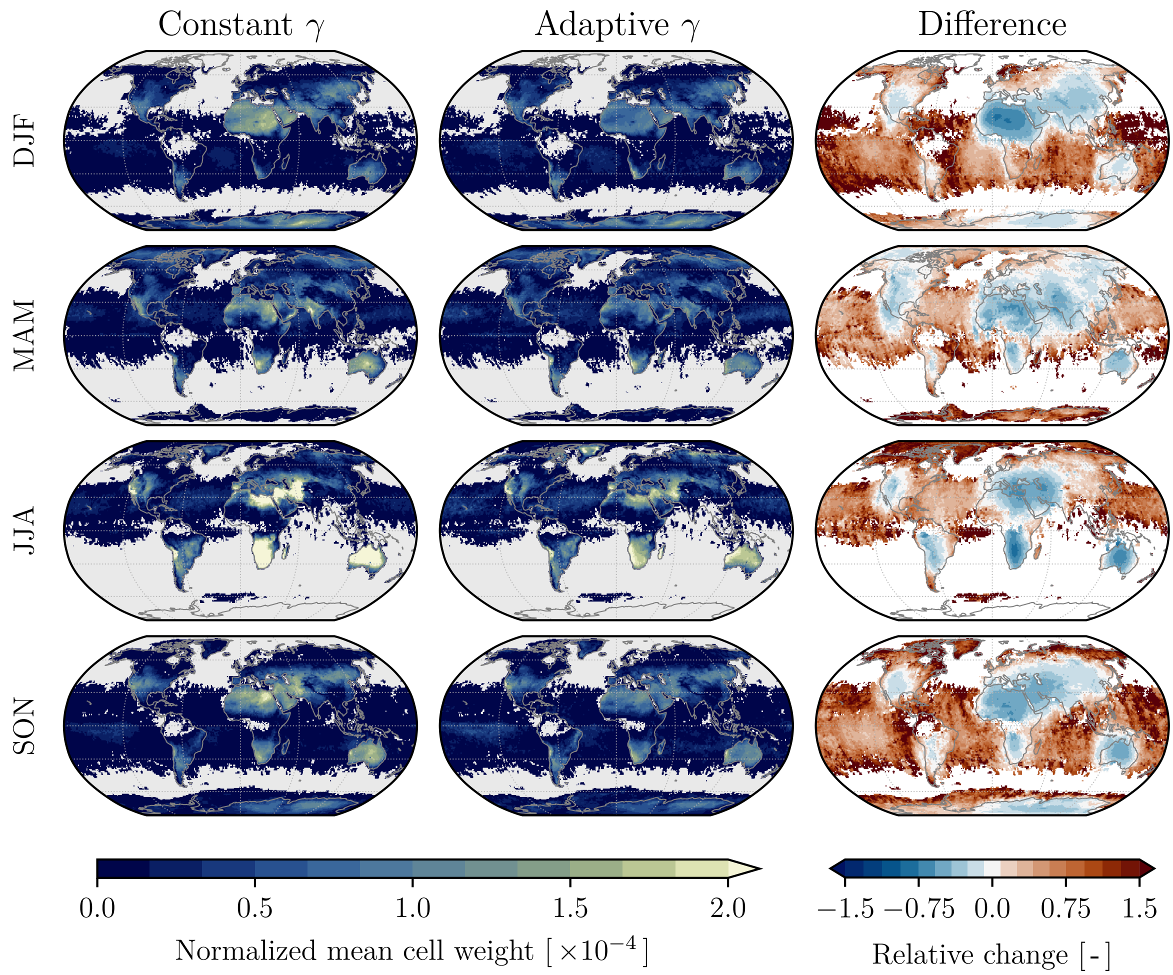

Figure 5. Seasonal comparison of normalized satellite weights over model grid cells, calculated as the sum of pixels per cell weighted by their individual regularization factor and normalized by the global total. The left column shows the constant regularization case; the middle column the parametric regularization; and the right column the symmetric relative change between them. The change is calculated from the logarithmic change as $h = \exp(|\ln(y/x)|) - 1$, obtaining a relative change that is symmetrical with respect to increases and decreases. For the constant regularization case, normalization implies that the relative cell weight depends only on the number of pixels per grid cell and not on the absolute magnitude of γ.

https://doi.org/10.5194/egusphere-2026-3458
Preprint. Discussion started: 28 August 2026

Table 3. Coefficient of variation of cell weights calculated over all grids. Results are from the seasonal average weights and annual mean (2019). Calculated as the standard deviation of cell weights normalized by their average. In the constant case, the coefficient of variation is independent of the absolute magnitude of γ.

Season	DJF	MAM	JJA	SON	2019
Constant γ	1.498	1.311	1.800	1.612	1.623
Parametric γ	1.253	1.126	1.396	1.286	1.305
Difference [%]	−17.9	−15.2	−25.4	−22.6	−21.8

in observational weighting directly influence the spatial distribution of information entering the inversion and, consequently, the inferred methane emissions discussed in the following section.

3.3 Inversion results

3.3.1 Cost function contribution

We compare how parametric regularization affects the satellite contribution to the cost function before and after optimization (Figure 6). To isolate the impact of satellite weighting, we examine satellite-only inversions (S2 and S3), excluding surface station data. In both cases, the spatial pattern of grid cells where the cost increases or decreases after optimization is similar. An increase in local cost (red on right column of Figure 6) means the model fit to satellite observations worsened in that region during optimization. This happens in the cases of (1) regions already well captured by the prior, where adjustments elsewhere indirectly introduce biases, or (2) low-weight regions where the inversion sacrifices local fit for global improvement.

Globally, both satellite-only inversions (S2 and S3) reduce the satellite cost term similarly; decreasing to 45.9% of its prior value (constant γ) and 50.6% (adaptive γ) respectively. Although the overall reduction is comparable, the spatial redistribution and local fit differ. In the Southern Hemisphere (SH) oceans and the Antarctic region, using the adaptive regularization produces a substantially smaller cost increase (lower values on the right column of Figure 6) than the constant regularization. This means that, percentually, a stronger weight over these regions limits the increase of the local cost function contribution. On the other hand, the stronger weight also means that the cost function values over these regions, before optimization, are higher than in the constant regularization case. Similarly, Northern high-latitude regions show a greater reduction in their mismatch with adaptive regularization. These results indicate that parametric regularization gives a more uniform global fit than a constant one, mainly by reducing cost increases in sparsely sampled regions.

https://doi.org/10.5194/egusphere-2026-3458
Preprint. Discussion started: 28 August 2026

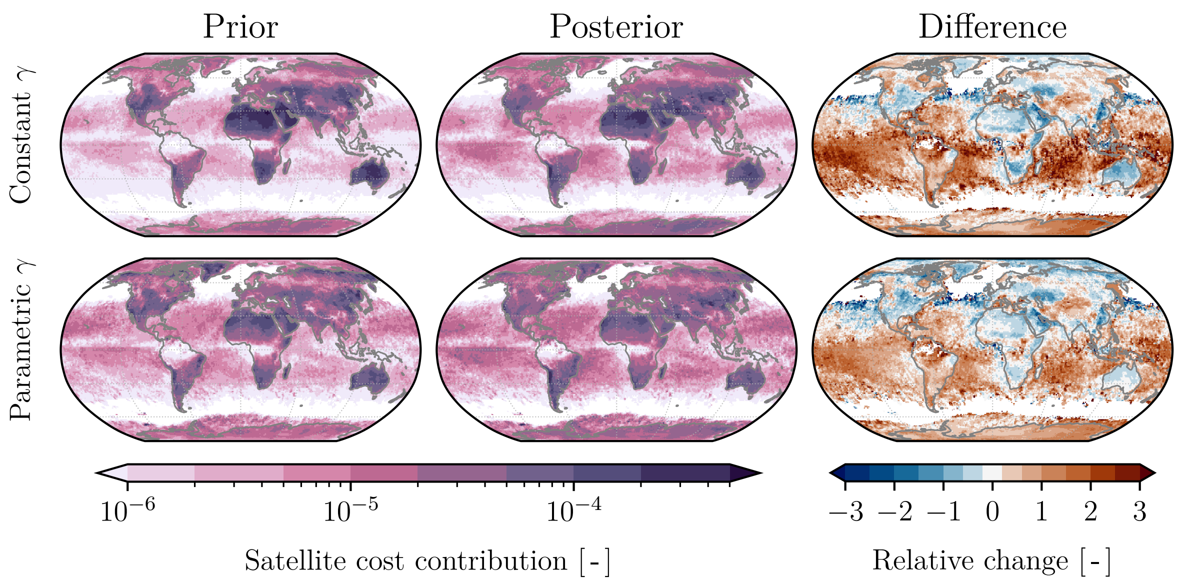

Figure 6. Satellite cost contribution per grid cell for satellite-only inversions with constant γ (S2) and parametric γ (S3). Values are the sum of individual sounding contributions to the cost function per grid cell. The right column shows the symmetric relative change between prior and posterior simulations. Absolute values are not directly comparable between configurations due to different initial total costs.

3.3.2 Emission adjustments

Following optimization, global total methane fluxes remain of similar magnitude across configurations and display broadly consistent spatial structures. However, regional differences emerge when comparing emission adjustments obtained with adaptive and constant regularization (see Figure 7).

When applying adaptive regularization, stronger emission increases are obtained over Southeast Asia, a region with multiple significant CH_4 sources (see Figure 7). In particular, fires in this region can be long-lasting and sustained by underground peat combustion (Di Giuseppe et al., 2018). Fire radiative power (FRP) or burned-area products primarily capture surface signals and may therefore miss low-intensity but persistent underground fires (Kaiser et al., 2012). These characteristics provide a possible explanation for the stronger emission adjustments obtained with adaptive regularization. While the inversion results alone cannot confirm this, the larger adjustments are consistent with biomass-burning emissions being underestimated in the prior fluxes, requiring larger corrections when higher cell weights are assigned through the parametric regularization, though further assessment would be necessary to validate this interpretation.

Southeastern Brazil also shows increased emission adjustments with the adaptive factor, particularly in regions where major urban areas, ports, and industries are located (Rio de Janeiro and São Paulo states). Although the increase in cell weight is concentrated on the summer months, weighting of nearby coastal observations may strengthen constraints on inland emissions through atmospheric transport. In contrast, Canada shows a substantial emission reduction with adaptive regularization. This

https://doi.org/10.5194/egusphere-2026-3458
Preprint. Discussion started: 28 August 2026

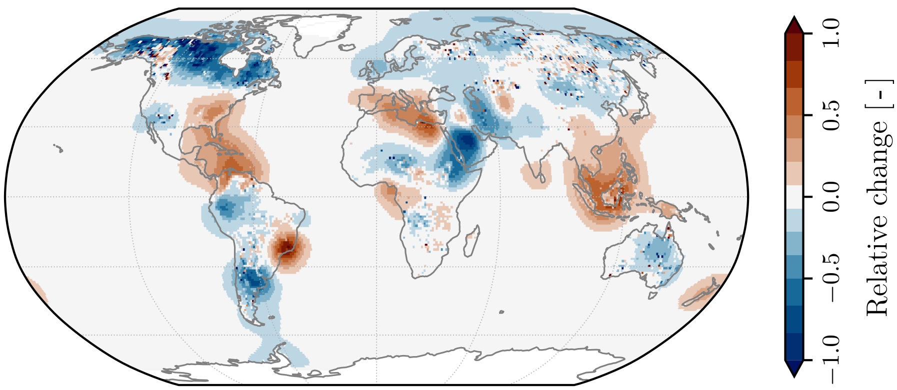

Figure 7. Symmetric relative change in optimized emission fluxes between satellite-only inversions using adaptive (S3) and constant (S2) regularization. Calculated using the ratio of posterior emissions from S3 and S2. Negative values indicate resulting lower emissions when using adaptive regularization.

region is dominated by wetland sources, which decrease in all simulation configurations. The higher local weight in the adaptive case leads to a stronger reduction in the local cost contribution, producing stronger emission adjustments.

More generally, the regional emission adjustments should not necessarily be interpreted as direct evidence of biases in the prior emissions. In weakly constrained regions, particularly those with larger emissions, the inversion has greater freedom to modify these emissions without strongly affecting the observational cost. Such regions may therefore act as garbage collectors for the inversion, absorbing part of the adjustment required to reconcile mismatches arising from more strongly constrained regions, where the observations more strongly penalize changes in emissions. Adaptive regularization seeks to reduce this effect by balancing the overall observational weight that individual grid cells hold. Consequently, relatively large differences when using the adaptive weighting in underconstrained regions may reflect the spatial distribution of observational constraints and the compensating behavior of the inversion, rather than a corresponding magnitude of error in the prior emissions.

Comparing the satellite-only (S3) and combined (S5) inversions highlights the influence of specific stations on emission adjustments (Figure 8). Major relative reductions are observed around PSA, BHD, MEX, and ASK, while clear annual emission increases appear around CBA, PAL, and SHM (see Figure 1). These reductions suggest differences between the constraints imposed by the satellite columns on the modeled vertical profiles and those imposed by surface mixing ratios from the stations. Such discrepancies can be attributed to the strong constraints that in situ measurements provide on near-surface concentrations, emphasizing the importance of including ground-based measurements in emission inversions. Additionally, biased initial CH_4 concentrations may contribute to over-corrections if the spin-up period is too short, as the inversion may compensate for mismatches in the atmospheric state.

Further, the budgets derived from the inversions were compared against the Global Methane Budget (GMB) top-down estimates (Figure 9). Our 2019 simulations align more closely with the 2020 emission estimates than with the 2010–2019 average. This likely reflects the relative stability of global methane emissions, making the decade average less representative of condi-

https://doi.org/10.5194/egusphere-2026-3458
Preprint. Discussion started: 28 August 2026

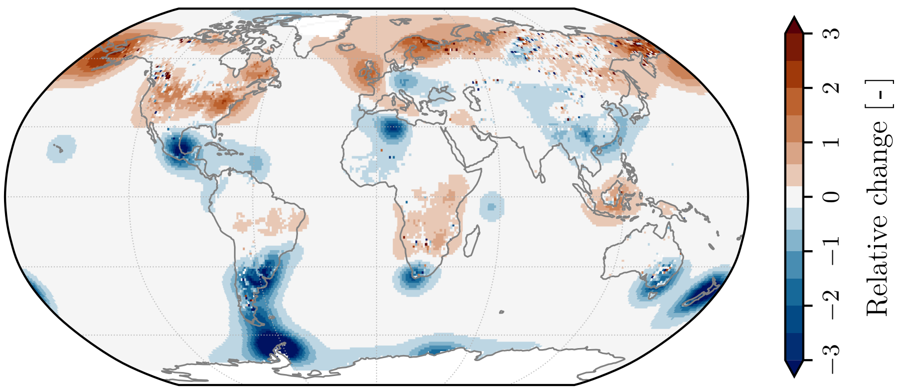

Figure 8. Symmetric relative change of emission fluxes resulting from including surface stations (S5) in the inversion using adaptive regularization (S3). Calculated using the ratio of optimized emissions from S5 and S3. Negative values indicate a decrease in emissions when in-situ measurements are assimilated.

tions in 2019 than the 2020 estimation. Exact agreement between individual categories is not expected due to methodological differences between the optimization methods.

3.3.3 Modeled atmosphere evaluation

To assess whether the resulting emission differences are consistent with independent observations, the inversion results are evaluated against TCCON column observations. A summary of all TCCON observations is provided in Table 4, showing the error-weighted RMSE and MBE, together with the averaged normalized mismatch (detailed results for each site are provided in Table S3). These metrics are calculated from the posterior emissions and the observations. Overall, the S1 inversion shows poorer agreement with TCCON observations, highlighting the value of including column observations in the inversions to provide constraints beyond the surface level. The metrics for the other simulations are relatively similar, although the adaptive cases show a slight tendency toward lower RMSE, MBE, and mismatch values.

Comparisons at specific sites are performed using sigma-normalized mismatches between posterior modeled and observed columns. Results for four sites, Eureka, Ny-Ålesund, Réunion, and Wollongong are shown in Figure 10. These sites were selected to illustrate two aspects of the inversion behavior, differences in satellite sampling, and the influence of nearby surface constraints. Ny-Ålesund, located at high northern latitudes near the Zeppelin station (ZEP), is characterized by relatively sparse satellite coverage and the presence of nearby surface measurements, leading to stronger local constraints in simulations that include NOAA observations. In contrast, Eureka, which is located at a similar latitude, does not have an immediate NOAA station, with Alert being the closest one. Réunion, located in the tropical Southern Hemisphere, lacks nearby surface measurements, while satellite observations are highly concentrated during the Southern Hemisphere summer. Finally, Wollongong is strongly influenced by satellite observations throughout the year, while the nearby Cape Grim station is sufficiently close to affect emissions and concentrations in the region.

https://doi.org/10.5194/egusphere-2026-3458
Preprint. Discussion started: 28 August 2026

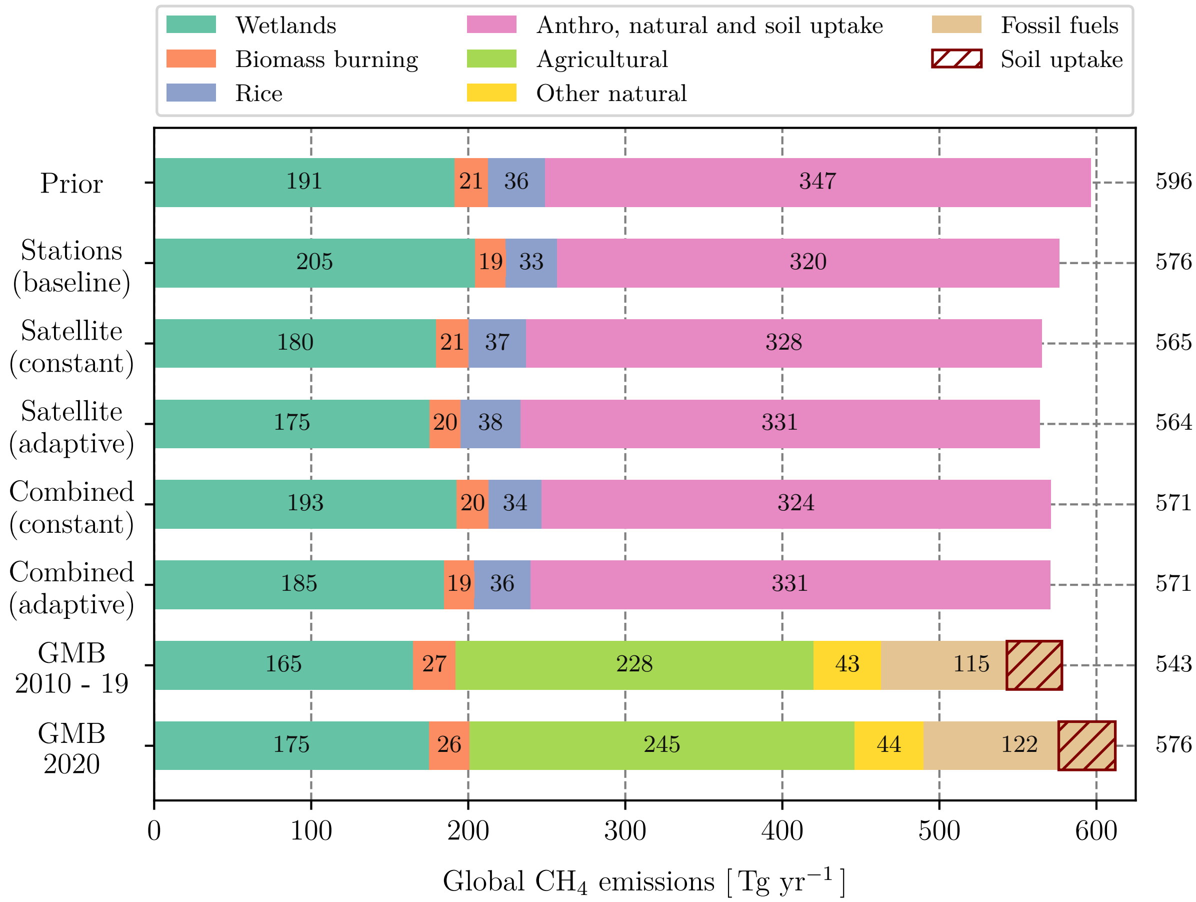

Figure 9. Comparison of global posterior budgets from each simulation against the a priori and data from the Global Methane Budget (GMB; Saunois et al. (2025)) top-down estimates. Values inside each bar represent the total of those emission categories, and the outer right column shows the sum of all categories. Soil uptake is included as a subtraction of the total for the GMB values (35 and 36 Tg yr^{-1}, respectively). In contrast, in this study, they were optimized together with anthropogenic and other natural sources.

https://doi.org/10.5194/egusphere-2026-3458
Preprint. Discussion started: 28 August 2026

Table 4. Summary of statistical metrics for the modeled results compared with TCCON observations. Note that none of the simulations assimilate these data.

	Simulation	Weighted RMSE	Weighted MBE	Normalized mismatch
S0	A priori	10.00	5.08	1.50
S1	Stations (baseline)	11.19	−7.51	−2.17
S2	Satellite (constant)	10.02	−6.97	−2.02
S3	Satellite (adaptive)	9.99	−6.64	−1.93
S4	Combined (constant)	10.02	−6.62	−1.92
S5	Combined (adaptive)	9.91	−6.45	−1.87

At Ny-Ålesund, the increased weight assigned to the satellite observations through adaptive regularization results in a decrease in the modeled columns. This behavior is consistently observed in both the satellite-only and combined inversions and persists across the other sites located above 50°N (see Figure S2). This bias is unlikely to originate from the satellite retrievals themselves, as validation of the WFMD v2.0 product against TCCON shows a slight positive bias at high northern latitudes (Schneising et al., 2026). Instead, the underestimation likely reflects errors introduced by transport or excessive chemical loss at high latitudes, possibly linked to uncertainties in OH fields, which remain a known challenge in methane inversions (Zhao et al., 2020, 2023; Naus et al., 2021, 2019; Lan et al., 2021). Seasonal coverage limitations at high latitudes, where retrievals are mostly available during summer, may also contribute to representativeness errors. At Eureka, although all simulations exhibit a positive bias in the modeled columns, the adaptive regularization still reduces the modeled columns relative to the corresponding constant-regularization cases.

At Réunion, located in the tropical Southern Hemisphere, there is a stronger underestimation of the total column. This bias is most pronounced in the baseline (S1) simulation. In the absence of a nearby in situ station, the satellite-only inversions show better agreement with the observations, reinforcing the importance of an extended background monitoring network for constraining inversions. In this region, the underestimation may also result from compensating effects, whereby an overly polluted modeled atmosphere is balanced by globally reduced emissions, leading to cleaner near-surface concentrations than those observed by either the satellite or TCCON. By comparison, at Wollongong, the negative model bias increases, although the agreement with TCCON improves more clearly when parametric weighting is applied, leading to better results in S3 and S5 than in their constant-regularization counterparts.

Validation against NOAA background stations further supports these findings. Posterior simulations generally reduce normalized mismatches relative to the a priori across most stations, as expected, since both the baseline and combined inversions assimilate these observations (see Figure S1). Overall, the simulations assimilating the satellite observations perform worse against NOAA flask measurements, with the discrepancy increasing when adaptive regularization is applied. This may be explained by the fact that neither the satellite nor the station observations are bias-corrected; therefore, they may be incon-

https://doi.org/10.5194/egusphere-2026-3458
Preprint. Discussion started: 28 August 2026

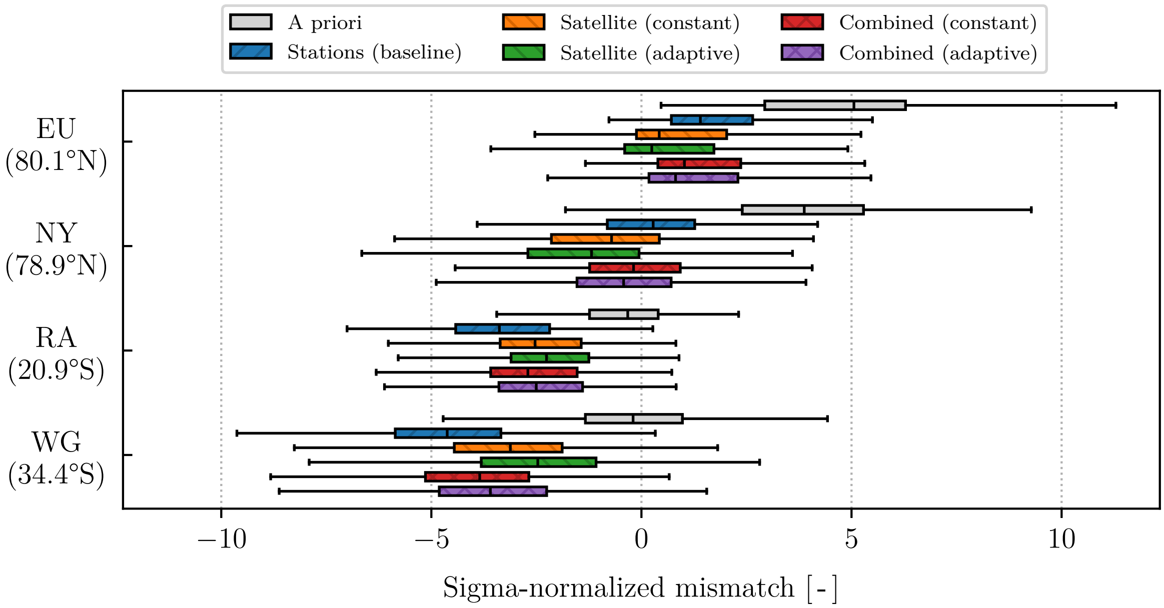

Figure 10. Sigma-normalized error between modeled columns and TCCON observations, calculated as the difference between the modeled total columns and TCCON observations divided by the observation uncertainty. A priori results are shown in gray for reference; all other bars correspond to posterior simulations after emission optimization. Results are shown for Eureka (Canada; $n = 1,337$), Ny-Ålesund (Svalbard; $n = 1,232$), Réunion (Indian Ocean; $n = 2,016$), and Wollongong (Australia; $n = 3,785$).

sistent and provide competing constraints. A more constrained problem has less freedom to simultaneously fit all available observations.

Consistent with the TCCON results, high-latitude stations (above 40°N) show the largest mismatches in the satellite-only (S2 and S3) inversions, where no surface measurements were assimilated. These mismatches appear as a negative model bias (i.e., an underestimation of CH_4 surface concentrations), which becomes more pronounced when adaptive regularization is applied. This suggests that the satellite observations represent a cleaner total column than that simulated by the model. In contrast, in the Southern Hemisphere, applying parametric regularization slightly increases the overestimation of surface concentrations, even when emissions near Antarctica are reduced. Overall, these results point to discrepancies between the modeled vertical profiles and the satellite observations, with the latter indicating a cleaner atmosphere.

Latitudinal band distributions from TROPOMI (see Figure S7) show that the model successfully captures the observed columns in the Northern Hemisphere, with relatively small biases across all simulations assimilating these data.

In the Southern Hemisphere, adaptive weighting increases modeled column mixing ratios, although this does not lead to the overestimation observed at the surface stations. Therefore, in this region, the model tends to produce a surface layer too polluted relative to the stations when assimilating only TROPOMI, while producing a total column that is too clean relative to the satellite observations when assimilating only surface observations. Both effects become more pronounced when per-

https://doi.org/10.5194/egusphere-2026-3458
Preprint. Discussion started: 28 August 2026

Table 5. Summary of statistical metrics for the modeled results compared with NOAA measurements. Note that both the baseline and combined inversions assimilate these measurements, logically yielding better fits than the satellite-only inversions.

	Simulation	Weighted RMSE	Weighted MBE	Normalized mismatch
S0	A priori	17.75	14.52	3.282
S1	Stations (baseline)	7.83	0.47	0.088
S2	Satellite (constant)	12.53	−0.22	−0.088
S3	Satellite (adaptive)	14.21	−0.16	−0.086
S4	Combined (constant)	8.52	1.41	0.293
S5	Combined (adaptive)	8.72	1.55	0.318

observation regularization factors are applied. A similar behavior can also be observed at WG, the southernmost TCCON site (see Figure 3). These results emphasize the importance of jointly assimilating surface and column observations with complementary sensitivities, thereby constraining the inversion to maintain a vertically consistent methane distribution that emerges from both the prior and the observational constraints through atmospheric transport.

The seasonal mismatch (see Figure S8) shows that the absolute mismatch is reduced in several regions when adaptive weighting is applied. However, the overall results remain consistent across inversion configurations, indicating that adaptive regularization produces emission estimates comparable to those obtained using different constant regularization values in previous studies.

4 Conclusions

In this study, we introduced a parametric approach for calculating regularization factors that weight the influence of individual satellite observations. By assigning observation-specific weights during preprocessing, the method provides more balanced assimilation of dense TROPOMI observations alongside relatively sparse in-situ measurements. We evaluated the approach using global methane inversions with the TM5-MP/4DVAR system.

Parametric regularization produces a more homogeneous spatial distribution of observational weights across the model grid. For TROPOMI observations in 2019, it reduced the relative variation in grid-cell weights by roughly 20% compared with a constant regularization approach. This redistribution increases the contribution of regions with sparse satellite coverage, such as oceans and high latitudes, while reducing the dominance of densely observed regions.

The adjusted weighting leads to regional differences in optimized methane fluxes. Although these changes are generally localized and moderate, noticeable differences occur in regions such as Southeast Asia and Canada, where the increased weighting of sparse observations strengthens constraints on emissions. Despite these regional variations, the resulting posterior methane budget for 2019 remains consistent with the latest Global Methane Budget estimates, aligning more closely with 2020 estimates than with the 2010–2019 average.

Evaluation against TCCON observations shows that parametric weighting preserves the overall behavior of the inversion. Persistent high-latitude biases likely originate from modeling limitations, including uncertainties in OH distributions, discrepancies between surface and column constraints, and difficulties in reproducing realistic vertical methane profiles. Further improvements may be achieved through longer model spin-up periods or through initial concentration fields that better match the modeled distribution.

Because the regularization weights are calculated as a preprocessing step, the covariance structure of the inversion remains fixed throughout the optimization, and the method introduces minimal computational overhead. This makes the approach easily applicable to other satellite retrieval products and inverse modeling frameworks, providing a flexible methodology for combining multiple satellite datasets within a single inversion system.

The advancing capabilities of new satellites with increased spatial resolution, together with the ability of parametric regularization to better characterize the distribution of methane and other trace gases from these observations, improve our ability to identify emission sources and, consequently, support the development of more effective climate policies.

Code and data availability. All simulations were performed using the inversion suit TMVar v1.2.6 (0717523) of the LAMOS group, and the model TM5-MP (82dd6175), both available at https://doi.org/10.5281/zenodo.20748931 (Parraguez Cerda et al., 2026). The TMVar inversion system includes the implementation of the adaptive weighting method described in this paper, together with the configurations for computing the weighting factors. Configuration files specific for every shown simulation are provided within the TMVar code.

The NOAA measurements were obtained from the Global Monitoring Laboratory data archive, available at https://gml.noaa.gov/ccgg/ (accessed on 5 April 2024). The L2 TROPOMI WFMD v2.0 product was obtained from the University of Bremen's Institute for Environmental Physics, available at https://www.iup.uni-bremen.de/carbon_ghg/ (accessed on 6 August 2025). The TCCON data were obtained from the TCCON Data Archive hosted by CaltechDATA at https://tccondata.org (accessed on 14 December 2024).

Author contributions. SPC, ND, MV, and MK contributed to the conceptualization of the study. SPC, JRN, ND, AS, OS, MV, and MK contributed to methodology and model setup. SPC, JRN, ND, and MK provided interpretation of data and results. SPC, JRN, AS, and OS did data processing. SPC performed all simulations, produced all results and figures, and wrote the original draft. ND, MV and MK contributed to the fund acquisition. All authors contributed with scientific discussions, read and agreed to the published version of the manuscript.

Competing interests. Authors have no competing interests to declare

https://doi.org/10.5194/egusphere-2026-3458
Preprint. Discussion started: 28 August 2026

Acknowledgements. The simulations and analysis of data were performed on the HPC cluster Aether at the University of Bremen, financed by DFG, within the scope of the Excellence Initiative.

The development of the TROPOMI/WFMD data product received funding from the European Space Agency (ESA) via the projects GHG-CCI+ and SMART-CH4 (ESA contract Nos 4000126450/19/I-NB and 4000142730/23/I-NS) and from the German Federal Ministry of Research, Technology and Space (BMFTR) within its project ITMS via grant 01 LK2103A. The TROPOMI/WFMD retrievals were performed on HPC facilities of the IUP, University of Bremen, funded under DFG/FUGG grant Nos INST 144/379-1 and INST 144/493-1.

This publication contains modified Copernicus Sentinel data (2018-2020). Sentinel-5 Precursor is an ESA mission implemented on behalf of the European Commission. The TROPOMI payload is a joint development by ESA and the Netherlands Space Office (NSO). The Sentinel-5 Precursor ground-segment development has been funded by ESA and with national contributions from The Netherlands, Germany, and Belgium.

Financial support. This research is funded by the Deutsche Forschungsgemeinschaft (DFG, German Research Foundation) under Germany's Excellence Strategy (University Allowance, EXC 2077, University of Bremen).

The article processing charges for this open-access publication were covered by the University of Bremen.

https://doi.org/10.5194/egusphere-2026-3458
Preprint. Discussion started: 28 August 2026

References

Bergamaschi, P., Krol, M., Dentener, F., Vermeulen, A., Meinhardt, F., Graul, R., Ramonet, M., Peters, W., and Dlugokencky, E. J.: Inverse modelling of national and European CH_4 emissions using the atmospheric zoom model TM5, Atmospheric Chemistry and Physics, 5, 2431–2460, https://doi.org/10.5194/acp-5-2431-2005, 2005.

Bergamaschi, P., Frankenberg, C., Meirink, J. F., Krol, M., Villani, M. G., Houweling, S., Frank, D., Edward, J. D., John, B. M., Luciana, V. G., Andreas, E., and Ingeborg, L.: Inverse modeling of global and regional CH_4 emissions using SCIAMACHY satellite retrievals, Journal of Geophysical Research Atmospheres, 114, 22 301, https://doi.org/10.1029/2009JD012287, 2009.

Bergamaschi, P., Krol, M., Meirink, J. F., Dentener, F., Segers, A., Van Aardenne, J., Monni, S., Vermeulen, A. T., Schmidt, M., Ramonet, M., Yver, C., Meinhardt, F., Nisbet, E. G., Fisher, R. E., O'Doherty, S., and Dlugokencky, E. J.: Inverse modeling of European CH_4 emissions 2001-2006, Journal of Geophysical Research Atmospheres, 115, 22 309, https://doi.org/10.1029/2010JD014180, 2010.

Bergamaschi, P., Houweling, S., Segers, A., Krol, M., Frankenberg, C., Scheepmaker, R. A., Dlugokencky, E., Wofsy, S. C., Kort, E. A., Sweeney, C., Schuck, T., Brenninkmeijer, C., Chen, H., Beck, V., and Gerbig, C.: Atmospheric CH_4 in the first decade of the 21st century: Inverse modeling analysis using SCIAMACHY satellite retrievals and NOAA surface measurements, Journal of Geophysical Research Atmospheres, 118, 7350–7369, https://doi.org/10.1002/JGRD.50480, 2013.

Brasseur, G. P. and Jacob, D. J.: Modeling of Atmospheric Chemistry, Cambridge University Press, ISBN 9781107146969, https://doi.org/10.1017/9781316544754, 2017.

Buchwitz, M., de Beek, R., Noël, S., Burrows, J. P., Bovensmann, H., Schneising, O., Khlystova, I., Bruns, M., Bremer, H., Bergamaschi, P., Körner, S., and Heimann, M.: Atmospheric carbon gases retrieved from SCIAMACHY by WFM-DOAS: version 0.5 CO and CH4 and impact of calibration improvements on CO_2 retrieval, Atmospheric Chemistry and Physics, 6, 2727–2751, https://doi.org/10.5194/acp-6-2727-2006, 2006.

Chevallier, F.: Impact of correlated observation errors on inverted CO_2 surface fluxes from OCO measurements, Geophysical Research Letters, 34, https://doi.org/10.1029/2007GL030463, 2007.

Cleveland, R. B., Cleveland, W. S., McRae, J. E., and Terpenning, I.: STL: A Seasonal-Trend Decomposition Procedure Based on LOESS, Journal of Official Statistics, 6, 3–73, 1990.

Connor, B. J., Boesch, H., Toon, G., Sen, B., Miller, C., and Crisp, D.: Orbiting Carbon Observatory: Inverse method and prospective error analysis, Journal of Geophysical Research, 113, https://doi.org/10.1029/2006JD008336, 2008.

Crippa, M., Guizzardi, D., Solazzo, E., Muntean, M., Schaaf, E., Monforti-Ferrario, F., Banja, M., Olivier, J., Grassi, G., Rossi, S., and Vignati, E.: GHG emissions of all world countries - 2021, Tech. rep., Joint Research Centre (JRC), European Comission, ISBN 978-92-76-41547-3, https://doi.org/10.2760/173513, 2021.

Di Giuseppe, F., Rémy, S., Pappenberger, F., and Wetterhall, F.: Using the Fire Weather Index (FWI) to improve the estimation of fire emissions from fire radiative power (FRP) observations, Atmospheric Chemistry and Physics, 18, 5359–5370, https://doi.org/10.5194/acp-18-5359-2018, 2018.

Dlugokencky, E. J., Steele, L. P., Lang, P. M., and Masarie, K. A.: The growth rate and distribution of atmospheric methane, Journal of Geophysical Research, 99, https://doi.org/10.1029/94JD01245, 1994.

Dlugokencky, E. J., Bruhwiler, L., White, J. W. C., Emmons, L. K., Novelli, P. C., Montzka, S. A., Masarie, K. A., Lang, P. M., Crotwell, A. M., Miller, J. B., and Gatti, L. V.: Observational constraints on recent increases in the atmospheric CH_4 burden, Geophysical Research Letters, 36, https://doi.org/10.1029/2009GL039780, 2009.

https://doi.org/10.5194/egusphere-2026-3458
Preprint. Discussion started: 28 August 2026

Dlugokencky, E. J., Nisbet, E. G., Fisher, R., and Lowry, D.: Global atmospheric methane: budget, changes and dangers, Philosophical Transactions of the Royal Society A: Mathematical, Physical and Engineering Sciences, 369, 2058–2072, https://doi.org/10.1098/rsta.2010.0341, 2011.

Doubalova, J. and Sindelarova, K.: Gridded CH4 emissions from termites, Tech. rep., Copernicus Atmosphere Monitoring Service (CAMS), 2018.

Eskes, H. J., Piters, A. J. M., Levelt, P. F., Allaart, M. A. F., and Kelder, H. M.: Variational Assimilation of GOME Total-Column Ozone Satellite Data in a 2D Latitude-Longitude Tracer-Transport Model, Journal of the Atmospheric Sciences, 56, 3560–3572, https://doi.org/10.1175/1520-0469(1999)056<3560:VAOGTC>2.0.CO;2, 1999.

Etiope, G., Ciotoli, G., Schwietzke, S., and Schoell, M.: Gridded maps of geological methane emissions and their isotopic signature, Earth System Science Data, 11, https://doi.org/10.5194/ESSD-11-1-2019, 2019.

Etminan, M., Myhre, G., Highwood, E. J., and Shine, K. P.: Radiative forcing of carbon dioxide, methane, and nitrous oxide: A significant revision of the methane radiative forcing, Geophysical Research Letters, 43, 12,614–12,623, https://doi.org/10.1002/2016GL071930, 2016.

Eyring, V., Gillett, N. P., Achuta Rao, K. M., Barimalala, R., Barreiro Parrillo, M., Bellouin, N., Cassou, C., Durack, P. J., Kosaka, Y., McGregor, S., Min, S., Morgenstern, O., and Sun, Y.: Human Influence on the Climate System, in: Climate Change 2021: The Physical Science Basis. Contribution of Working Group I to the Sixth Assessment Report of the Intergovernmental Panel on Climate Change, edited by Masson-Delmotte, V., Zhai, P., Pirani, A., Connors, S. L., Péan, C., Berger, S., Caud, N., Chen, Y., Goldfarb, L., Gomis, M. I., Huang, M., Leitzell, K., Lonnoy, E., Matthews, J. B. R., Maycock, T. K., Waterfield, T., Yelekçi, O., Yu, R., and Zhou, B., pp. 423–552, Cambridge University Press, https://doi.org/10.1017/9781009157896.005, 2021.

Forster, P., Storelvmo, T., Armour, K., Collins, W., Dufresne, J.-L., Frame, D., Lunt, D. J., Mauritsen, T., Palmer, M. D., Watanabe, M., Wild, M., and Zhang, H.: The Earth's Energy Budget, Climate Feedbacks and Climate Sensitivity, in: Climate Change 2021: The Physical Science Basis. Contribution of Working Group I to the Sixth Assessment Report of the Intergovernmental Panel on Climate Change, edited by Masson-Delmotte, V., Zhai, P., Pirani, A., Connors, S. L., Péan, C., Berger, S., Caud, N., Chen, Y., Goldfarb, L., Gomis, M. I., Huang, M., Leitzell, K., Lonnoy, E., Matthews, J. B. R., Maycock, T. K., Waterfield, T., Yelekçi, O., Yu, R., and Zhou, B., pp. 923–1054, Cambridge University Press, https://doi.org/10.1017/9781009157896.009, 2021.

Frankenberg, C., Meirink, J. F., Bergamaschi, P., Goede, A. P. H., Heimann, M., Körner, S., Platt, U., van Weele, M., and Wagner, T.: Satellite chartography of atmospheric methane from SCIAMACHY on board ENVISAT: Analysis of the years 2003 and 2004, Journal of Geophysical Research: Atmospheres, 111, 7303, https://doi.org/10.1029/2005JD006235, 2006.

Gilbert, J. C. and Lemaréchal, C.: Some numerical experiments with variable-storage quasi-Newton algorithms, Mathematical Programming, 45, 407–435, https://doi.org/10.1007/BF01589113, 1989.

Hansen, P. C.: The L-Curve and its Use in the Numerical Treatment of Inverse Problems, in: Computational Inverse Problems in Electrocardiology, edited by Johnston, P., vol. 4, pp. 119–142, WIT Press, 2000.

Hersbach, H., Bell, B., Berrisford, P., Hirahara, S., Horányi, A., Muñoz-Sabater, J., Nicolas, J., Peubey, C., Radu, R., Schepers, D., Simmons, A., Soci, C., Abdalla, S., Abellan, X., Balsamo, G., Bechtold, P., Biavati, G., Bidlot, J., Bonavita, M., De Chiara, G., Dahlgren, P., Dee, D., Diamantakis, M., Dragani, R., Flemming, J., Forbes, R., Fuentes, M., Geer, A., Haimberger, L., Healy, S., Hogan, R. J., Hólm, E., Janisková, M., Keeley, S., Laloyaux, P., Lopez, P., Lupu, C., Radnoti, G., de Rosnay, P., Rozum, I., Vamborg, F., Villaume, S., and Thépaut, J. N.: The ERA5 global reanalysis, Quarterly Journal of the Royal Meteorological Society, 146, 1999–2049, https://doi.org/10.1002/qj.3803, 2020.

https://doi.org/10.5194/egusphere-2026-3458
Preprint. Discussion started: 28 August 2026

Hooghiemstra, P. B., Krol, M. C., Meirink, J. F., Bergamaschi, P., van der Werf, G. R., Novelli, P. C., Aben, I., and Röckmann, T.: Optimizing global CO emission estimates using a four-dimensional variational data assimilation system and surface network observations, Atmospheric Chemistry and Physics, 11, 4705–4723, https://doi.org/10.5194/acp-11-4705-2011, 2011.

Hooghiemstra, P. B., Krol, M. C., Bergamaschi, P., de Laat, A. T. J., van der Werf, G. R., Novelli, P. C., Deeter, M. N., Aben, I., and Röckmann, T.: Comparing optimized CO emission estimates using MOPITT or NOAA surface network observations, Journal of Geophysical Research: Atmospheres, 117, https://doi.org/10.1029/2011JD017043, 2012.

Houweling, S., Kaminski, T., Dentener, F., Lelieveld, J., and Heimann, M.: Inverse modeling of methane sources and sinks using the adjoint of a global transport model, Journal of Geophysical Research Atmospheres, 104, 26 137–26 160, https://doi.org/10.1029/1999JD900428, 1999.

Huijnen, V., Flemming, J., Chabrillat, S., Errera, Q., Christophe, Y., Blechschmidt, A. M., Richter, A., and Eskes, H.: C-IFS-CB05-BASCOE: Stratospheric chemistry in the Integrated Forecasting System of ECMWF, Geoscientific Model Development, 9, 3071–3091, https://doi.org/10.5194/gmd-9-3071-2016, 2016.

Inness, A., Ades, M., Agustí-Panareda, A., Barr, J., Benedictow, A., Blechschmidt, A. M., Jose Dominguez, J., Engelen, R., Eskes, H., Flemming, J., Huijnen, V., Jones, L., Kipling, Z., Massart, S., Parrington, M., Peuch, V. H., Razinger, M., Remy, S., Schulz, M., and Suttie, M.: The CAMS reanalysis of atmospheric composition, Atmospheric Chemistry and Physics, 19, 3515–3556, https://doi.org/10.5194/acp-19-3515-2019, 2019.

Jacob, D. J., Turner, A. J., Maasakkers, J. D., Sheng, J., Sun, K., Liu, X., Chance, K., Aben, I., McKeever, J., and Frankenberg, C.: Satellite observations of atmospheric methane and their value for quantifying methane emissions, Atmospheric Chemistry and Physics, 16, 14 371–14 396, https://doi.org/10.5194/acp-16-14371-2016, 2016.

Jacob, D. J., Varon, D. J., Cusworth, D. H., Dennison, P. E., Frankenberg, C., Gautam, R., Guanter, L., Kelley, J., McKeever, J., Ott, L. E., Poulter, B., Qu, Z., Thorpe, A. K., Worden, J. R., and Duren, R. M.: Quantifying methane emissions from the global scale down to point sources using satellite observations of atmospheric methane, Atmospheric Chemistry and Physics, 22, 9617–9646, https://doi.org/10.5194/acp-22-9617-2022, 2022.

Kaiser, J. W., Heil, A., Andreae, M. O., Benedetti, A., Chubarova, N., Jones, L., Morcrette, J.-J., Razinger, M., Schultz, M. G., Suttie, M., and van der Werf, G. R.: Biomass burning emissions estimated with a global fire assimilation system based on observed fire radiative power, Biogeosciences, 9, 527–554, https://doi.org/10.5194/bg-9-527-2012, 2012.

Kirschke, S., Bousquet, P., Ciais, P., Saunois, M., Canadell, J. G., Dlugokencky, E. J., Bergamaschi, P., Bergmann, D., Blake, D. R., Bruhwiler, L., Cameron-Smith, P., Castaldi, S., Chevallier, F., Feng, L., Fraser, A., Heimann, M., Hodson, E. L., Houweling, S., Josse, B., Fraser, P. J., Krummel, P. B., Lamarque, J. F., Langenfelds, R. L., Le Quéré, C., Naik, V., O'doherty, S., Palmer, P. I., Pison, I., Plummer, D., Poulter, B., Prinn, R. G., Rigby, M., Ringeval, B., Santini, M., Schmidt, M., Shindell, D. T., Simpson, I. J., Spahni, R., Steele, L. P., Strode, S. A., Sudo, K., Szopa, S., Van Der Werf, G. R., Voulgarakis, A., Van Weele, M., Weiss, R. F., Williams, J. E., and Zeng, G.: Three decades of global methane sources and sinks, Nature Geoscience, 6, 813–823, https://doi.org/10.1038/ngeo1955, 2013.

Kopacz, M., Jacob, D. J., Fisher, J. A., Logan, J. A., Zhang, L., Megretskaia, I. A., Yantosca, R. M., Singh, K., Henze, D. K., Burrows, J. P., Buchwitz, M., Khlystova, I., McMillan, W. W., Gille, J. C., Edwards, D. P., Eldering, A., Thouret, V., and Nedelec, P.: Global estimates of CO sources with high resolution by adjoint inversion of multiple satellite datasets (MOPITT, AIRS, SCIAMACHY, TES), Atmospheric Chemistry and Physics, 10, 855–876, https://doi.org/10.5194/acp-10-855-2010, 2010.

Krol, M., Houweling, S., Bregman, B., van den Broek, M., Segers, A., van Velthoven, P., Peters, W., Dentener, F., and Bergamaschi, P.: The two-way nested global chemistry-transport zoom model TM5: Algorithm and applications, Atmospheric Chemistry and Physics, 5, 417–432, https://doi.org/10.5194/acp-5-417-2005, 2005.

Krol, M., Peters, W., Hooghiemstra, P., George, M., Clerbaux, C., Hurtmans, D., McInerney, D., Sedano, F., Bergamaschi, P., El Hajj, M., Kaiser, J. W., Fisher, D., Yershov, V., and Muller, J.-P.: How much CO was emitted by the 2010 fires around Moscow?, Atmospheric Chemistry and Physics, 13, 4737–4747, https://doi.org/10.5194/acp-13-4737-2013, 2013.

Kuze, A., Suto, H., Shiomi, K., Kawakami, S., Tanaka, M., Ueda, Y., Deguchi, A., Yoshida, J., Yamamoto, Y., Kataoka, F., Taylor, T. E., and Buijs, H. L.: Update on GOSAT TANSO-FTS performance, operations, and data products after more than 6 years in space, Atmospheric Measurement Techniques, 9, 2445–2461, https://doi.org/10.5194/amt-9-2445-2016, 2016.

Lambert, G. and Schmidt, S.: Reevaluation of the oceanic flux of methane: Uncertainties and long term variations, Chemosphere, 26, 579–589, https://doi.org/10.1016/0045-6535(93)90443-9, 1993.

Lan, X., Basu, S., Schwietzke, S., Bruhwiler, L. M., Dlugokencky, E. J., Michel, S. E., Sherwood, O. A., Tans, P. P., Thoning, K., Etiope, G., Zhuang, Q., Liu, L., Oh, Y., Miller, J. B., Pétron, G., Vaughn, B. H., and Crippa, M.: Improved Constraints on Global Methane Emissions and Sinks Using δ13C-CH4, Global Biogeochemical Cycles, 35, https://doi.org/10.1029/2021GB007000, 2021.

Lindqvist, H., Kivimäki, E., Häkkilä, T., Tsuruta, A., Schneising, O., Buchwitz, M., Lorente, A., Martinez Velarte, M., Borsdorff, T., Alberti, C., Backman, L., Buschmann, M., Chen, H., Dubravica, D., Hase, F., Heikkinen, P., Karppinen, T., Kivi, R., McGee, E., Notholt, J., Rautiainen, K., Roche, S., Simpson, W., Strong, K., Tu, Q., Wunch, D., Aalto, T., and Tamminen, J.: Evaluation of Sentinel-5P TROPOMI Methane Observations at Northern High Latitudes, Remote Sensing, 16, 2979, https://doi.org/10.3390/rs16162979, 2024.

Liu, Z. and Rabier, F.: The potential of high-density observations for numerical weather prediction: A study with simulated observations, Quarterly Journal of the Royal Meteorological Society, 129, 3013–3035, https://doi.org/10.1256/qj.02.170, 2003.

Lorente, A., Borsdorff, T., Butz, A., Hasekamp, O., Aan De Brugh, J., Schneider, A., Wu, L., Hase, F., Kivi, R., Wunch, D., Pollard, D. F., Shiomi, K., Deutscher, N. M., Velazco, V. A., Roehl, C. M., Wennberg, P. O., Warneke, T., and Landgraf, J.: Methane retrieved from TROPOMI: Improvement of the data product and validation of the first 2 years of measurements, Atmospheric Measurement Techniques, 14, 665–684, https://doi.org/10.5194/amt-14-665-2021, 2021.

Lu, X., Jacob, D. J., Zhang, Y., Maasakkers, J. D., Sulprizio, M. P., Shen, L., Qu, Z., Scarpelli, T. R., Nesser, H., Yantosca, R. M., Sheng, J., Andrews, A., Parker, R. J., Boesch, H., Anthony Bloom, A., and Ma, S.: Global methane budget and trend, 2010–2017: complementarity of inverse analyses using in situ (GLOBALVIEWplus CH4 ObsPack) and satellite (GOSAT) observations, Atmospheric Chemistry and Physics, 21, 4637–4657, https://doi.org/10.5194/acp-21-4637-2021, 2021.

Maasakkers, J. D., Jacob, D. J., Sulprizio, M. P., Scarpelli, T. R., Nesser, H., Sheng, J. X., Zhang, Y., Hersher, M., Anthony Bloom, A., Bowman, K. W., Worden, J. R., Janssens-Maenhout, G., and Parker, R. J.: Global distribution of methane emissions, emission trends, and OH concentrations and trends inferred from an inversion of GOSAT satellite data for 2010-2015, Atmospheric Chemistry and Physics, 19, 7859–7881, https://doi.org/10.5194/acp-19-7859-2019, 2019.

Meirink, J. F., Bergamaschi, P., and Krol, M. C.: Four-Dimensional Variational data assimilation for inverse modelling of atmospheric methane emissions: Method and comparison with synthesis inversion, Atmospheric Chemistry and Physics, 8, 6341–6353, https://doi.org/10.5194/acp-8-6341-2008, 2008.

Naus, S., Montzka, S. A., Pandey, S., Basu, S., Dlugokencky, E. J., and Krol, M.: Constraints and biases in a tropospheric two-box model of OH, Atmospheric Chemistry and Physics, 19, 407–424, https://doi.org/10.5194/acp-19-407-2019, 2019.

Naus, S., Montzka, S. A., Patra, P. K., and Krol, M. C.: A three-dimensional-model inversion of methyl chloroform to constrain the atmospheric oxidative capacity, Atmospheric Chemistry and Physics, 21, 4809–4824, https://doi.org/10.5194/acp-21-4809-2021, 2021.

Naus, S., Domingues, L. G., Krol, M., Luijkx, I. T., Gatti, L. V., Miller, J. B., Gloor, E., Basu, S., Correia, C., Koren, G., Worden, H. M., Flemming, J., Pétron, G., and Peters, W.: Sixteen years of MOPITT satellite data strongly constrain Amazon CO fire emissions, Atmospheric Chemistry and Physics, 22, 14 735–14 750, https://doi.org/10.5194/acp-22-14735-2022, 2022.

Nechita-Banda, N., Krol, M., van der Werf, G. R., Kaiser, J. W., Pandey, S., Huijnen, V., Clerbaux, C., Coheur, P., Deeter, M. N., and Röckmann, T.: Monitoring emissions from the 2015 Indonesian fires using CO satellite data, Philosophical Transactions of the Royal Society B: Biological Sciences, 373, 20170 307, https://doi.org/10.1098/rstb.2017.0307, 2018.

Nüß, J. R., Daskalakis, N., Piwowarczyk, F. G., Gkouvousis, A., Schneising, O., Buchwitz, M., Kanakidou, M., Krol, M. C., and Vrekoussis, M.: Top-down CO emission estimates using TROPOMI CO data in the TM5-4DVAR (r1258) inverse modeling suit, Geoscientific Model Development, 18, 2861–2890, https://doi.org/10.5194/gmd-18-2861-2025, 2025.

Parraguez Cerda, S., Nüß, J. R., Daskalakis, N., Segers, A., Vrekoussis, M., and Kanakidou, M.: TMVar (TM5-MP/4DVAR) inverse modeling suit with extensions for adaptive weighting of TROPOMI WFMD product , https://doi.org/10.5281/zenodo.20748931, 2026.

Paton-Walsh, C., Emmerson, K. M., Garland, R. M., Keywood, M., Hoelzemann, J. J., Huneeus, N., Buchholz, R. R., Humphries, R. S., Altieri, K., Schmale, J., Wilson, S. R., Labuschagne, C., Kalisa, E., Fisher, J. A., Deutscher, N. M., van Zyl, P. G., Beukes, J. P., Joubert, W., Martin, L., Mkololo, T., Barbosa, C., de Fatima Andrade, M., Schofield, R., Mallet, M. D., Harvey, M. J., Formenti, P., Piketh, S. J., and Olivares, G.: Key challenges for tropospheric chemistry in the Southern Hemisphere, Elementa: Science of the Anthropocene, 10, https://doi.org/10.1525/ELEMENTA.2021.00050, 2022.

Qu, Z., Jacob, D. J., Shen, L., Lu, X., Zhang, Y., Scarpelli, T. R., Nesser, H., Sulprizio, M. P., Maasakkers, J. D., Bloom, A. A., Worden, J. R., Parker, R. J., and Delgado, A. L.: Global distribution of methane emissions: a comparative inverse analysis of observations from the TROPOMI and GOSAT satellite instruments, Atmospheric Chemistry and Physics, 21, 14 159–14 175, https://doi.org/10.5194/acp-21-14159-2021, 2021.

Ridgwell, A. J., Marshall, S. J., and Gregson, K.: Consumption of atmospheric methane by soils: A process-based model, Global Biogeochemical Cycles, 13, 59–70, https://doi.org/10.1029/1998GB900004, 1999.

Rijsdijk, P., Eskes, H., Dingemans, A., Boersma, K. F., Sekiya, T., Miyazaki, K., and Houweling, S.: Quantifying uncertainties in satellite NO_2 super-observations for data assimilation and model evaluation, Geoscientific Model Development, 18, 483–509, https://doi.org/10.5194/gmd-18-483-2025, 2025.

Sanderson, M. S.: Biomass of termites and their emissions of methane and carbon dioxide: A global database, Global Biogeochemical Cycles, 10, 543–557, https://doi.org/10.1029/96GB01893, 1996.

Saunois, M., Stavert, A. R., Poulter, B., Bousquet, P., Canadell, J. G., Jackson, R. B., Raymond, P. A., Dlugokencky, E. J., Houweling, S., Patra, P. K., Ciais, P., Arora, V. K., Bastviken, D., Bergamaschi, P., Blake, D. R., Brailsford, G., Bruhwiler, L., M. Carlson, K., Carrol, M., Castaldi, S., Chandra, N., Crevoisier, C., M. Crill, P., Covey, K., L. Curry, C., Etiope, G., Frankenberg, C., Gedney, N., I. Hegglin, M., Höglund-Isaksson, L., Hugelius, G., Ishizawa, M., Ito, A., Janssens-Maenhout, G., M. Jensen, K., Joos, F., Kleinen, T., B. Krummel, P., L. Langenfelds, R., G. Laruelle, G., Liu, L., Machida, T., Maksyutov, S., C. McDonald, K., McNorton, J., A. Miller, P., R. Melton, J., Morino, I., Müller, J., Murguia-Flores, F., Naik, V., Niwa, Y., Noce, S., O'Doherty, S., J. Parker, R., Peng, C., Peng, S., P. Peters, G., Prigent, C., Prinn, R., Ramonet, M., Regnier, P., J. Riley, W., A. Rosentreter, J., Segers, A., J. Simpson, I., Shi, H., J. Smith, S., Paul Steele, L., F. Thornton, B., Tian, H., Tohjima, Y., N. Tubiello, F., Tsuruta, A., Viovy, N., Voulgarakis, A., S. Weber, T., Van Weele, M., R. Van Der Werf, G., F. Weiss, R., Worthy, D., Wunch, D., Yin, Y., Yoshida, Y., Zhang, W., Zhang, Z., Zhao, Y., Zheng, B., Zhu, Q., Zhu, Q., and Zhuang, Q.: The Global Methane Budget 2000-2017, Earth System Science Data, 12, 1561–1623, https://doi.org/10.5194/ESSD-12-1561-2020, 2020.

Saunois, M., Martinez, A., Poulter, B., Zhang, Z., Raymond, P. A., Regnier, P., Canadell, J. G., Jackson, R. B., Patra, P. K., Bousquet, P., Ciais, P., Dlugokencky, E. J., Lan, X., Allen, G. H., Bastviken, D., Beerling, D. J., Belikov, D. A., Blake, D. R., Castaldi, S., Crippa, M., Deemer, B. R., Dennison, F., Etiope, G., Gedney, N., Höglund-Isaksson, L., Holgerson, M. A., Hopcroft, P. O., Hugelius, G., Ito, A., Jain, A. K., Janardanan, R., Johnson, M. S., Kleinen, T., Krummel, P. B., Lauerwald, R., Li, T., Liu, X., Mcdonald, K. C., Melton, J. R., Mühle, J., Müller, J., Murguia-Flores, F., Niwa, Y., Noce, S., Pan, S., Parker, R. J., Peng, C., Ramonet, M., Riley, W. J., Rocher-Ros, G., Rosentreter, J. A., Sasakawa, M., Segers, A., Smith, S. J., Stanley, E. H., Thanwerdas, J., Tian, H., Tsuruta, A., Tubiello, F. N., Weber, T. S., Van Der Werf, G. R., Worthy, D. E., Xi, Y., Yoshida, Y., Zhang, W., Zheng, B., Zhu, Q., Zhu, Q., and Zhuang, Q.: Global Methane Budget 2000-2020, Earth System Science Data, 17, 1873–1958, https://doi.org/10.5194/essd-17-1873-2025, 2025.

Schneising, O., Buchwitz, M., Reuter, M., Bovensmann, H., Burrows, J. P., Borsdorff, T., Deutscher, N. M., Feist, D. G., Griffith, D. W., Hase, F., Hermans, C., Iraci, L. T., Kivi, R., Landgraf, J., Morino, I., Notholt, J., Petri, C., Pollard, D. F., Roche, S., Shiomi, K., Strong, K., Sussmann, R., Velazco, V. A., Warneke, T., and Wunch, D.: A scientific algorithm to simultaneously retrieve carbon monoxide and methane from TROPOMI onboard Sentinel-5 Precursor, Atmospheric Measurement Techniques, 12, 6771–6802, https://doi.org/10.5194/amt-12-6771-2019, 2019.

Schneising, O., Buchwitz, M., Hachmeister, J., Vanselow, S., Reuter, M., Buschmann, M., Bovensmann, H., and Burrows, J. P.: Advances in retrieving XCH4 and XCO from Sentinel-5 Precursor: Improvements in the scientific TROPOMI/WFMD algorithm, Atmospheric Measurement Techniques, 16, 669–694, https://doi.org/10.5194/amt-16-669-2023, 2023.

Schneising, O., Bovensmann, H., Buchwitz, M., Buschmann, M., Deutscher, N. M., Griffith, D. W. T., Hachmeister, J., Hase, F., Iraci, L. T., Kivi, R., Morino, I., Ohyama, H., Petri, C., Reuter, M., Robinson, J., Roehl, C., Sha, M. K., Shiomi, K., Strong, K., Sussmann, R., Té, Y., Velazco, V. A., Vrekoussis, M., Wang, W., Warneke, T., Weidmann, D., Wunch, D., Zhou, M., and Bösch, H.: TROPOMI/WFMD v2.0: Improved retrievals of XCH_4 and XCO with XGBoost-based quality filtering, Atmospheric Measurement Techniques, 19, 2407–2435, https://doi.org/10.5194/amt-19-2407-2026, 2026.

Segers, A., van Peet, J., Nanni, R., Chevallier, F., and Houweling, S.: Description of the CH_4 inversion production chain, Tech. rep., Copernicus Atmosphere Monitoring Service (CAMS), https://confluence.ecmwf.int/display/CKB/Description+of+the+CH4+inversion+production+chain, [*accessed on 12 February 2026*], 2025.

Seinfeld, J. H. and Pandis, S. N.: Atmospheric Chemistry and Physics: From Air Pollution to Climate Change, Wiley-Blackwell, 3 edn., ISBN 978-1-118-94740-1, 2016.

Sheather, S. J. and Jones, M. C.: A Reliable Data-based Bandwidth Selection Method for Kernel Density Estimation, Journal of the Royal Statistical Society Series B: Statistical Methodology, 53, 683–690, https://doi.org/10.1111/j.2517-6161.1991.tb01857.x, 1991.

Silverman, B.: Density Estimation for Statistics and Data Analysis, Routledge, 1st edn., ISBN 9781315140919, https://doi.org/10.1201/9781315140919, 1986.

Simonin, D., Waller, J. A., Ballard, S. P., Dance, S. L., and Nichols, N. K.: A pragmatic strategy for implementing spatially correlated observation errors in an operational system: An application to Doppler radial winds, Quarterly Journal of the Royal Meteorological Society, 145, 2772–2790, https://doi.org/10.1002/qj.3592, 2019.

Szopa, S., Naik, V., Adhikary, B., Artaxo, P., Berntsen, T., Collins, W. D., Fuzzi, S., Gallardo, L., Kiendler-Scharr, A., Klimont, Z., Liao, H., Unger, N., and Zanis, P.: Short-Lived Climate Forcers, in: Climate Change 2021: The Physical Science Basis. Contribution of Working

https://doi.org/10.5194/egusphere-2026-3458
Preprint. Discussion started: 28 August 2026

Group I to the Sixth Assessment Report of the Intergovernmental Panel on Climate Change, chap. 6, pp. 817–922, Cambridge University Press, Cambridge, United Kingdom, https://doi.org/10.1017/9781009157896.008, 2021.

Talagrand, O. and Courtier, P.: Variational Assimilation of Meteorological Observations With the Adjoint Vorticity Equation. I: Theory, Quarterly Journal of the Royal Meteorological Society, 113, 1311–1328, https://doi.org/10.1002/QJ.49711347812, 1987.

Turner, A. J., Frankenberg, C., and Kort, E. A.: Interpreting contemporary trends in atmospheric methane, Proceedings of the National Academy of Sciences, 116, 2805–2813, https://doi.org/10.1073/pnas.1814297116, 2019.

Veefkind, J. P., Aben, I., McMullan, K., Förster, H., de Vries, J., Otter, G., Claas, J., Eskes, H. J., de Haan, J. F., Kleipool, Q., van Weele, M., Hasekamp, O., Hoogeveen, R., Landgraf, J., Snel, R., Tol, P., Ingmann, P., Voors, R., Kruizinga, B., Vink, R., Visser, H., and Levelt, P. F.: TROPOMI on the ESA Sentinel-5 Precursor: A GMES mission for global observations of the atmospheric composition for climate, air quality and ozone layer applications, Remote Sensing of Environment, 120, 70–83, https://doi.org/10.1016/j.rse.2011.09.027, 2012.

Williams, J. E., Boersma, K. F., Le Sager, P., and Verstraeten, W. W.: The high-resolution version of TM5-MP for optimized satellite retrievals: description and validation, Geoscientific Model Development, 10, 721–750, https://doi.org/10.5194/gmd-10-721-2017, 2017.

Wunch, D., Toon, G. C., Wennberg, P. O., Wofsy, S. C., Stephens, B. B., Fischer, M. L., Uchino, O., Abshire, J. B., Bernath, P., Biraud, S. C., Blavier, J.-F. F., Boone, C., Bowman, K. P., Browell, E. V., Campos, T., Connor, B. J., Daube, B. C., Deutscher, N. M., Diao, M., Elkins, J. W., Gerbig, C., Gottlieb, E., Griffith, D. W., Hurst, D. F., Jiménez, R., Keppel-Aleks, G., Kort, E. A., MacAtangay, R., MacHida, T., Matsueda, H., Moore, F., Morino, I., Park, S., Robinson, J., Roehl, C. M., Sawa, Y., Sherlock, V., Sweeney, C., Tanaka, T., and Zondlo, M. A.: Calibration of the Total Carbon Column Observing Network using aircraft profile data, Atmospheric Measurement Techniques, 3, 1351–1362, https://doi.org/10.5194/amt-3-1351-2010, 2010.

Wunch, D., Toon, G. C., Blavier, J.-F. L., Washenfelder, R. A., Notholt, J., Connor, B. J., Griffith, D. W. T., Sherlock, V., and Wennberg, P. O.: The Total Carbon Column Observing Network, Philosophical Transactions of the Royal Society A: Mathematical, Physical and Engineering Sciences, 369, 2087–2112, https://doi.org/10.1098/rsta.2010.0240, 2011.

Zhang, Y., Jacob, D. J., Maasakkers, J. D., Sulprizio, M. P., Sheng, J. X., Gautam, R., and Worden, J.: Monitoring global tropospheric OH concentrations using satellite observations of atmospheric methane, Atmospheric Chemistry and Physics, 18, 15 959–15 973, https://doi.org/10.5194/acp-18-15959-2018, 2018.

Zhang, Y., Jacob, D. J., Lu, X., Maasakkers, J. D., Scarpelli, T. R., Sheng, J.-X., Shen, L., Qu, Z., Sulprizio, M. P., Chang, J., Bloom, A. A., Ma, S., Worden, J., Parker, R. J., and Boesch, H.: Attribution of the accelerating increase in atmospheric methane during 2010–2018 by inverse analysis of GOSAT observations, Atmospheric Chemistry and Physics, 21, 3643–3666, https://doi.org/10.5194/acp-21-3643-2021, 2021.

Zhang, Z., Zimmermann, N. E., Kaplan, J. O., and Poulter, B.: Modeling spatiotemporal dynamics of global wetlands: Comprehensive evaluation of a new sub-grid TOPMODEL parameterization and uncertainties, Biogeosciences, 13, 1387–1408, https://doi.org/10.5194/bg-13-1387-2016, 2016.

Zhang, Z., Poulter, B., Feldman, A. F., Ying, Q., Ciais, P., Peng, S., and Li, X.: Recent intensification of wetland methane feedback, Nature Climate Change, 13, 430–433, https://doi.org/10.1038/s41558-023-01629-0, 2023.

Zhao, Y., Saunois, M., Bousquet, P., Lin, X., Berchet, A., Hegglin, M. I., Canadell, J. G., Jackson, R. B., Dlugokencky, E. J., Langenfelds, R. L., Ramonet, M., Worthy, D., and Zheng, B.: Influences of hydroxyl radicals (OH) on top-down estimates of the global and regional methane budgets, Atmospheric Chemistry and Physics, 20, 9525–9546, https://doi.org/10.5194/acp-20-9525-2020, 2020.

Zhao, Y., Saunois, M., Bousquet, P., Lin, X., Hegglin, M. I., Canadell, J. G., Jackson, R. B., and Zheng, B.: Reconciling the bottom-up and top-down estimates of the methane chemical sink using multiple observations, Atmospheric Chemistry and Physics, 23, 789–807, https://doi.org/10.5194/acp-23-789-2023, 2023.